The genome of a Bacteroidetes inhabitant of the human gut encodes a structurally distinct enoyl-acyl carrier protein reductase (FabI)

Received for publication, March 4, 2020, and in revised form, April 20, 2020 Published, Papers in Press, April 21, 2020, DOI 10.1074/jbc.RA120.013336

Christopher D. Radka[‡], Matthew W. Frank[‡], Jiangwei Yao[‡1], Jayaraman Seetharaman[§], Darcie J. Miller[§], and Charles O. Rock[‡2]

From the Departments of [‡]Infectious Diseases and [§]Structural Biology, St. Jude Children's Research Hospital, Memphis, Tennessee 38105

Edited by Wolfgang Peti

Enoyl-acyl carrier protein reductase (FabI) catalyzes a rate-controlling step in bacterial fatty-acid synthesis and is a target for antibacterial drug development. A phylogenetic analysis shows that FabIs fall into four divergent clades. Members of clades 1–3 have been structurally and biochemically characterized, but the fourth clade, found in members of phylum Bacteroidetes, is uncharacterized. Here, we identified the unique structure and conformational changes that distinguish clade 4 FabIs. *Alistipes finegoldii* is a prototypical Bacteroidetes inhabitant of the gut microbiome. We found that *A. finegoldii* FabI (*Af*FabI) displays cooperative kinetics and uses NADH as a cofactor, and its crystal structure at 1.72 Å resolution showed that it adopts a Rossmann fold as do other characterized FabIs. It also disclosed a carboxyl-terminal extension that forms a helix–helix interaction that links the protomers as a unique feature of *Af*FabI. An *Af*FabI·NADH crystal structure at 1.86 Å resolution revealed that this feature undergoes a large conformational change to participate in covering the NADH-binding pocket and establishing the water channels that connect the active site to the central water well. Progressive deletion of these interactions led to catalytically compromised proteins that fail to bind NADH. This unique conformational change imparted a distinct shape to the *Af*FabI active site that renders it refractory to a FabI drug that targets clade 1 and 3 pathogens. We conclude that the clade 4 FabI, found in the Bacteroidetes inhabitants of the gut, have several structural features and conformational transitions that distinguish them from other bacterial FabIs.

Bacterial fatty acid biosynthesis (FASII[3]) consists of a conserved collection of individual proteins that produce the fatty acids required for membrane phospholipid biogenesis (1). The FASII substrates are linked to acyl carrier protein (ACP)[3] and undergo successive rounds of condensation, reduction, dehydration, and reduction to extend the acyl chain by two carbons with each elongation cycle (Fig. 1*A*). The final reduction step of each elongation cycle is catalyzed by enoyl-ACP reductase (ENR) (Fig. 1*A*). There are two widely distributed, distinct ENR protein families, FabI and FabK (2–5). FabI proteins use NAD(P)H as the reductant and belong to the short-chain dehydrogenase superfamily of enzymes that use a Rossmann fold to bind the nucleotide cofactor (6, 7). Most short-chain dehydrogenases have an active site dyad consisting of Tyr-*X*aa$_3$-Lys, but the bacterial FabI subfamily is distinguished by having a differently spaced catalytic dyad consisting of Tyr-*X*aa$_6$-Lys (8, 9). FabK is a flavoprotein (FMN) that belongs to the NAD(P)H-dependent flavin oxidoreductase family (4). FabK adopts an overall TIM barrel fold (4, 5) and requires NAD(P)H as a reductant (2), but how the NADP(P)H and FMN cofactors collaborate in catalysis is not clear (3, 5). There are also two FabI-like ENRs (FabL and FabV) with a limited distribution in bacteria (10–14). These two reductases also belong to the short-chain dehydrogenase superfamily but are distantly related to FabI. The function of ENR in the FASII pathway is to pull each cycle of elongation to completion and is the rate-determining step of fatty acid elongation (15).

The role of ENR as a pacemaker of the essential FASII pathway has made it the subject of intense investigation as a target for antibiotic drug discovery (16, 17). AFN-1252 (afabicin (Debio 1452)) is the most clinically advanced of these compounds and is designed to specifically target staphylococcal FabI (18–21). Most commonly used, broad-spectrum antibiotics not only attack the pathogen but also devastate the commensal gut microbiome, leading to multiple complications (22, 23). As a pathogen-specific antibiotic (16), AFN-1252 has the desirable property of having no effect on the size or composition of the gut microbiome during therapy (24). Firmicutes and Bacteroidetes are the two most abundant bacterial phyla in the gut microbiome. Most Firmicutes (85%) are in Class Clostridia that encode *fabK* and not *fabI* (25), therefore these organisms are expected to be refractory to growth inhibition by FabI-targeted drugs (2, 3). The Bacteroidetes occupants of the gut microbiome are more diverse. Some contain only a *fabI* homo-

This work was supported by NIGMS, National Institutes of Health Grant GM034496 (to C. O. R.), Cancer Center Support Grant CA21765, and the American Lebanese Syrian Associated Charities. The authors declare that they have no conflicts of interest with the contents of this article. The content is solely the responsibility of the authors and does not necessarily represent the official views of the National Institutes of Health.

[1] Present address: General Dynamics Information Technology, 2 Corporate Blvd. NE, Atlanta, GA 30329.

[2] To whom correspondence should be addressed: 262 Danny Thomas Place, Memphis, TN 38105. Tel.: 901-595-3491; E-mail: charles.rock@stjude.org.

[3] The abbreviations used are: ACP, acyl carrier protein; ENR, enoyl-ACP reductase; RMSD, root mean square deviation; FabI, enoyl-(acyl-carrier-protein) reductase; FabK, enoyl-ACP reductase II; FASII, bacterial type II fatty acid synthesis; InhA, *M. tuberculosis* enoyl-(acyl-carrier-protein) reductase.

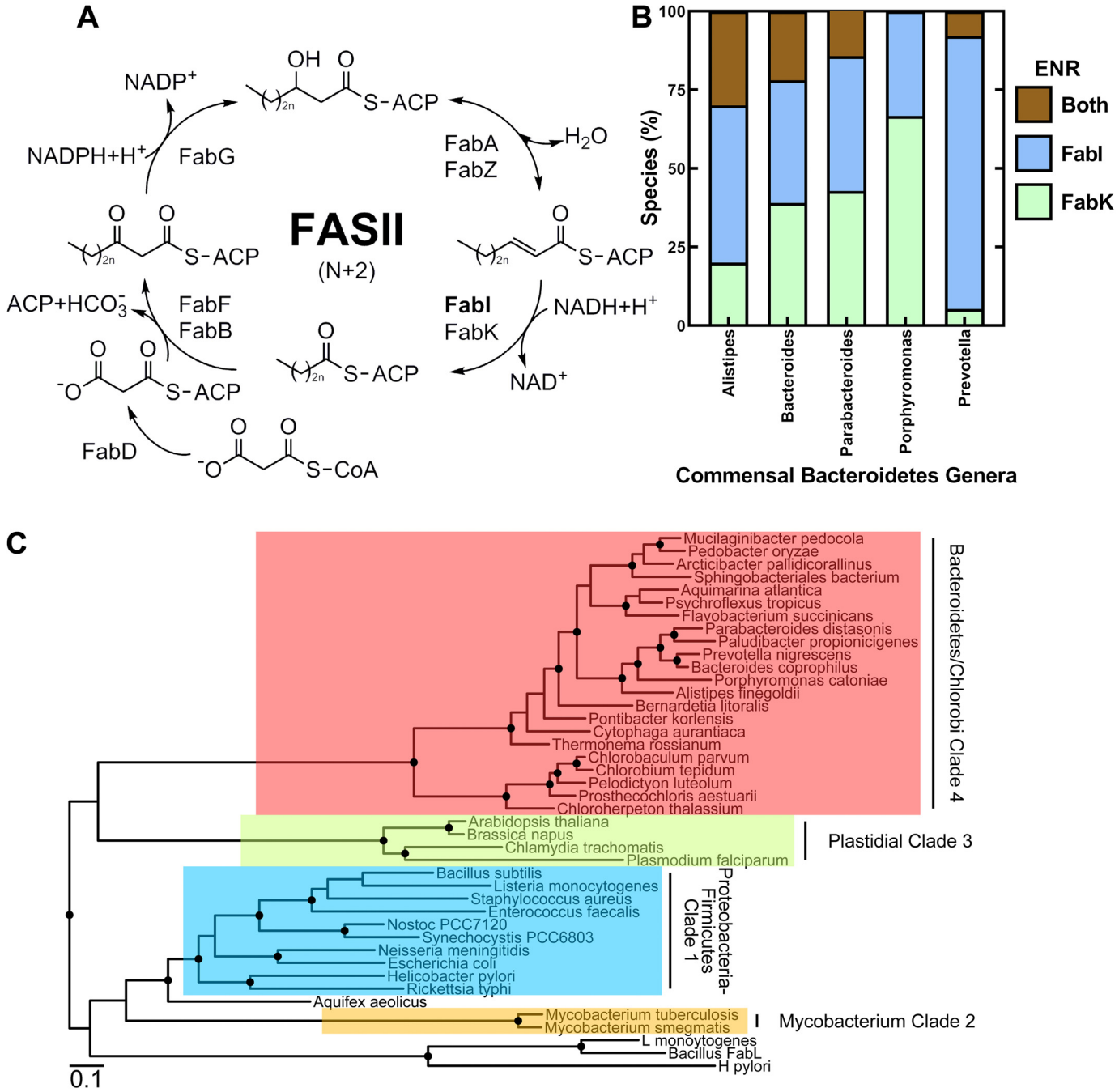

Figure 1. Enoyl-ACP reductases in the Bacteroidetes. *A*, a diagram of the four-step elongation cycle of bacterial fatty acid synthesis (FASII). The acyl chains are covalently bound to ACP and are extended by two carbons with each turn of the cycle. The final step is catalyzed by an enoyl-ACP reductase that catalyzes the reduction of *trans*-2-acyl–ACP to acyl-ACP. FabI and FabK are two widely distributed enoyl reductase protein families. *B*, the percentage of individual species encoding FabI, FabK, or both, in five abundant human-associated Bacteroidetes genera (*Alistipes*, $n = 10$; *Bacteroides*, $n = 41$; *Parabacteroides*, $n = 7$; *Porphyromonas*, $n = 15$; *Prevotella*, $n = 38$). *C*, evolutionary relationship between the FabI family sequences. The distantly related FabL sequences were used to root the tree. FabI proteins fall into four clades: clade 1, prototypical Proteobacteria/Firmicute proteins; clade 2, Mycobacteria proteins; clade 3, plastidial enzymes; and clade 4, Bacteroidetes/Chlorobi enzymes.

log, some contain only a *fabK* homolog, and some contain both a *fabI* and *fabK* (Fig. 1*B*). This bioinformatic analysis suggests that some commensal Bacteroidetes may be susceptible to FabI-targeted therapeutics. We constructed a phylogenetic tree to understand the evolutionary relationships between the FabIs expressed in bacteria (Fig. 1*C*). This analysis shows that there are four distinct FabI clades. Representative FabIs from clades 1–3 have been biochemically and structurally characterized. Bacteroidetes/Chlorobi phyla are in the fourth FabI clade, suggesting that Bacteroidetes FabI may have unique features not found in structures from the other clades.

The goal of this study was to structurally and functionally characterize the FabI from *Alistipes finegoldii* (*Af*FabI), a human Bacteroidetes commensal anaerobe containing a clade 4 FabI. Like other FabIs, *Af*FabI is a tetramer and adopts a Rossmann fold to bind the nucleotide cofactor. The unique feature

of *Af*FabI is the carboxyl-terminal α9 helix that forms a coiled-coil structure with the α9 helix of an adjacent protomer to form a protomer-protomer contact that is absent in the other three FabI clades. Upon NADH binding, the intertwined α9–α9 helices unravel to form a structured loop that is involved in sealing the lid over the active site of the opposite protomer. Deletion of the unique carboxyl-terminal domain results in a folded, but inactive enzyme because of severely compromised NADH affinity. The *Af*FabI active site uses the same Tyr-*X*aa$_6$-Lys catalytic dyad as other FabIs, but the surrounding residues create a unique active site environment that renders *Af*FabI refractory to a FabI therapeutic (AFN-1252) that effectively targets the clade 1 and 3 FabIs.

Results

Bioinformatics

The distribution of species in Bacteroidetes taxa encoding FabI, FabK, or both, was determined by counting the high homology FabI and FabK TBLASTN hits for each unique species entry in the RefSeq Representative Genomes database (12/22/2019) using the *Alistipes* FabI and FabK sequences and an e-value cut-off of 1e-100 for each hit. Environmental Bacteroidetes species encode for FabI only, FabK only, or both (not shown). Likewise, the individual species in the five major human-associated Bacteroidetes genera (*Alistipes*, *Bacteroides*, *Parabacteroides*, *Porphyromonas*, and *Prevotella*) encode for one of the three possible combinations of FabI and FabK (Fig. 1*B*). *Prevotella*, a prominent genus of the gut microbiome, had the highest number of species that encode only a FabI, but all three possible combinations were found in the individual species from all the commensal Bacteroidetes genera. A phylogenetic analysis was conducted to understand the evolutionary relationships between the FabIs (Fig. 1*C*). Clade 1 FabIs are encoded in the Proteobacteria and Firmicute phyla and are represented by the prototypical *Escherichia coli* (26) and *Staphylococcus aureus* (27) crystal structures. Clade 2 are the mycobacterial enzymes typified by the structure of InhA of *Mycobacterium tuberculosis* (28). Clade 3 FabIs consist of the plastid FabIs and include the structurally characterized FabIs of *Chlamydia trachomatis* (29) and *Plasmodium falciparum* (30). The FabI sequences from the closely related Bacteroidetes and Chlorobi phyla form a distinct fourth clade (Fig. 1*C*). The phylogenetic relationship between the various Bacteroidetes/Chlorobi FabI sequences is in overall agreement with the phylogenetic relationships between the organisms based on their 16S RNA sequences (31). These data show that Bacteroidetes/Chlorobi clade 4 FabIs have a divergent evolutionary history from the other clades, suggesting that there may be structural and/or functional differences between clade 4 FabIs and the other three characterized clades.

A. finegoldii FabI and FabK

We selected *A. finegoldii* as a prototypical gut commensal bacterium to examine the properties of the clade 4 FabIs. *A. finegoldii* is predicted to have both a FabI and FabK. *A. finegoldii* FabI (*Af*FabI) (UniProt ID: A0A174E195) has 32% identity with *Neisseria gonorrheae* FabI. The *A. finegoldii* FabK (*Af*FabK) (UniProt ID: I3YI65) has 42% identity with *Streptococcus pneumoniae* FabK and contains the signature FMN-binding motif. The ENR functions of *Af*FabI and *Af*FabK were verified by determining whether plasmids directing their synthesis would complement *E. coli* strain JP1111 (*fabI*(Ts)) (Fig. 2, *A* and *B*). The positive controls for the experiment were strain JP1111 carrying plasmids expressing *E. coli* FabI (*Ec*FabI), *C. trachomatis* FabI (*Ct*FabI), or *Clostridium acetobutylicum* FabK (*Ca*FabK), and the negative control was the expression vector lacking a gene insert. All strains grew at the permissive temperature (30 °C) (Fig. 2*A*). Strain JP1111 containing the empty vector failed to grow at the nonpermissive temperature (42 °C), whereas the plasmids expressing *Af*FabI, *Af*FabK, and all the positive controls grew at 42 °C (Fig. 2*B*). These data show that *A. finegoldii* encodes both a FabI and FabK ENR as predicted from the bioinformatic analyses.

AFN-1252 is a FabI inhibitor that is known to inhibit clade 1 and clade 3 FabIs (29, 32, 33). The sensitivity of *Af*FabI (clade 4) to AFN-1252 was compared with other FabIs using *E. coli* strain ANS1 (Δ*tolC*) expressing a series of FabIs as described previously (33). Strain ANS1 was transformed with a series of plasmids expressing different FabI and FabK enzymes and the AFN-1252 minimal inhibitory concentrations were determined using a microbroth dilution assay (Fig. 2*C*). Growth of strains ANS1/p*Ec*FabI (clade 1) and ANS1/p*Ct*FabI (clade 3) were both inhibited by AFN-1252 whereas all strains expressing a FabK were refractory to AFN-1252 growth inhibition. A key result was that strain ANS1/p*Af*FabI was refractory to AFN-1252 inhibition indicating that clade 4 FabIs may have an active site that is distinct from the clade 1 and clade 3 proteins.

Biochemical properties of AfFabI

An amino-terminal His-tagged version of *Af*FabI was expressed in *E. coli* and purified by affinity and gel filtration chromatography to obtain a homogeneous 34-kDa protein based on SDS gel electrophoresis (Fig. 3*A*, *inset*). *Af*FabI eluted as a single species on the calibrated XBridge BEH SEC column (Fig. 3*A*). Its Stokes radius was consistent with a molecular weight of 145 kDa (Fig. 3*A*, *inset*), indicating that like other characterized FabI proteins *Af*FabI exists as a tetramer (theoretical molecular weight 136 kDa) (7). Sedimentation velocity analysis confirmed *Af*FabI exists as a homotetramer in solution with an s_{20} value of 6.59 S corresponding to 141 kDa protein (Fig. 3*B*). *Af*FabI exhibited high-affinity, cooperative binding to NADH. The K_D was estimated by surface plasmon resonance to be 225 nM with a Hill coefficient of 1.6 (Fig. 3*C*). The *Af*FabI affinity for its reaction product NAD^+ was estimated in similar surface plasmon resonance experiments to be orders of magnitude lower (K_D = 1.623 ± 0.008 mM) than for NADH (not shown). NADH increased the stability of *Af*FabI to thermal denaturation by 7 °C (Fig. 3*D*). These data indicated that NADH binding results in a more stable protein structure.

*Af*FabI enzymatic activity of NADH oxidation to NAD^+ was monitored by spectrophotometry at 340 nm. *Af*FabI catalyzed the oxidation of NADH to NAD^+ in the presence of crotonyl-CoA (Fig. 4*A*). The NADH apparent $K_{0.5}$ was 22.3 ± 4.6 μM at 1.25 mM crotonyl-CoA and NADH exhibited positive cooperative behavior with a Hill number of 2.4 ± 0.2 (Fig. 4*B*). NADPH did not support the reaction (Fig. 4*A*, *inset*). Cooperative bind-

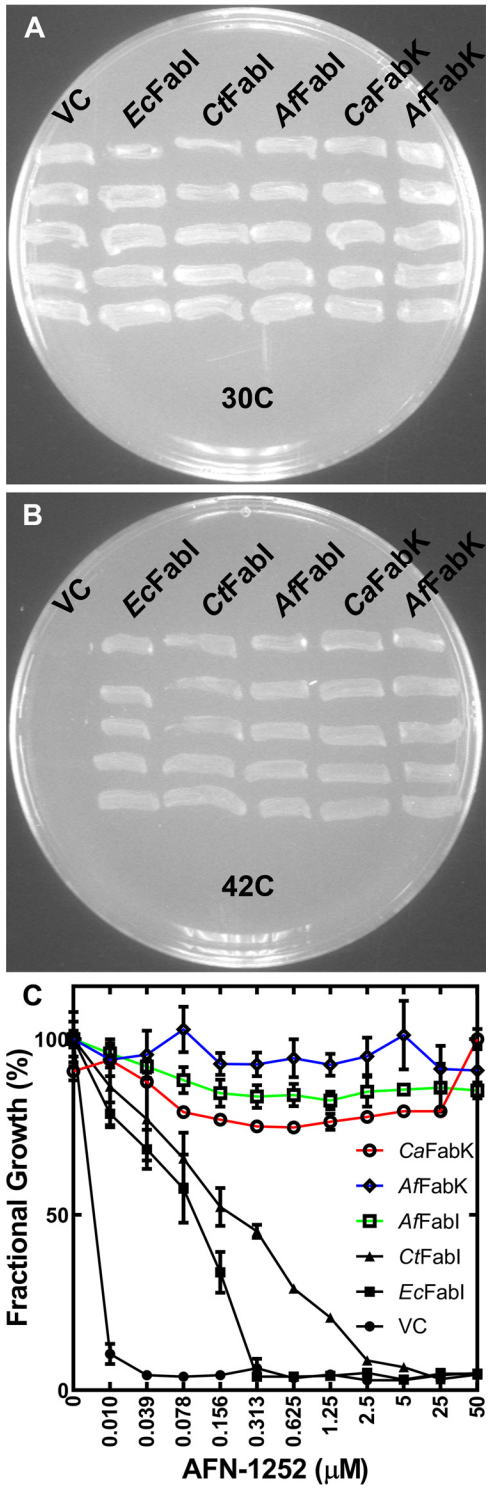

Figure 2. *A. finegoldii* encodes two functional enoyl-acyl carrier protein reductases. *A*, growth of temperature-sensitive *E. coli* strain JP1111 (*fabI*(Ts)) mutant transformed with empty plasmid vector control (*VC*), or plasmids expressing either *E. coli* FabI (*Ec*FabI), *C. trachomatis* FabI (*Ct*FabI), *A. finegoldii* FabI (*Af*FabI; UniProt ID: A0A174E195), *C. acetobutylicum* FabK (*Ca*FabK), or *A. finegoldii* FabK (*Af*FabK; UniProt ID: I3YI65) under the growth-permissive temperature (30 °C). *B*, growth of the same strain set at the nonpermissive temperature (42 °C). Five biological replicates were tested for each strain. *C*, microbroth dilution assay to rank the sensitivities of the FabIs and FabKs to AFN-1252 by determining the minimal inhibitory concentrations for AFN-1252 against *E. coli* strain ANS1 (Δ*tolC*) (33) transformed with the same series of plasmids described in *panel A*. Mean ± S.E. ($n = 3$).

ing of the reduced nicotinamide substrate is characteristic of FabIs and has been studied in detail with *S. aureus* FabI (34). The crotonyl-CoA $K_{0.5}$ was 457 ± 45 μM and exhibited some cooperative behavior with a Hill number of 1.5 (Fig. 4*C*). Mass spectrometry analysis confirmed that butyryl-CoA was the product in the enzymatic reaction (Fig. 4*C*, *inset*). These data demonstrate *Af*FabI catalyzes the FASII ENR reaction and that *Af*FabI exhibits kinetic properties that are like other characterized FabI enzymes. Although triclosan inhibited *Af*FabI with an IC_{50} of 1.76 ± 0.57 μM, which was similar to triclosan inhibition of *Ec*FabI (35), *Af*FabI was refractory to AFN-1252 inhibition (Fig. 4*D*), suggesting its active site was significantly different from the active sites in the clade 1 and clade 3 FabIs that are sensitive to this drug.

The AfFabI crystal structure

The 1.72 Å *Af*FabI structure was refined to R/R_{free} 20.6/24.5 (Table 1). Two protomers were in the asymmetric unit and are similar to each other with a Cα RMSD of 0.34 Å across 260 residues. The protomers interact with two symmetry-related protomers around a crystallographic 2-fold axis to create the tetramer. The presence of tetramers in the crystal is consistent with the gel filtration and sedimentation experiments. The unique *Af*FabI protomer feature is α9, a carboxyl-terminal helix that protrudes from the α/β core structure that is absent in the clade 1–3 enzymes (Fig. 5*A*). Structural alignment of *Af*FabI protomer (lacking α9) with *Ec*FabI (PDB ID: 5CFZ) (36, 81) showed the two structures are near identical with a Cα RMSD of 1.48 Å across 448 residues. Like the clade 1–3 FabIs (7), the *Af*FabI protomer consists of a seven-stranded parallel β-sheet flanked by three α helices on either side that adopts a Rossmann fold for dinucleotide substrate binding (Fig. 5*A*). The signature Tyr-*X*aa$_6$-Lys FabI catalytic dyad places the active site in the same location as other FabIs (8, 9). FabI is a dimer of dimers with three molecular 2-fold noncrystallographic symmetry axes (*P*, *Q*, and *R*) along the subunit interfaces (27, 38, 39) (Fig. 5*B*). Each protomer has a total surface area of ~13,400 Å^2, and ~4800 Å^2 (~36%) is buried upon tetramerization. These values are similar to other FabIs (28, 36, 40–42, 81). There are two disordered regions in the structure. The residues constituting the putative α6 active site lid (Thr-197 to Gly-209) were expected to be absent from the model because the flexible lid is only resolved in FabI·NAD(P)H binary complexes in other FabI clades (27, 43, 44). The second unstructured region is the final 13 amino acids of the carboxyl terminus.

FabI tetramers are stabilized by extensive intermolecular interactions along the protomer interfaces with conserved dimerization and tetramerization interfaces (27, 38, 45). Like clade 1–3 FabIs, *Af*FabI dimerization occurs along the *P* axis interface and consists of interacting helices α8 and strands β7 linking the A/B or C/D protomers (Fig. 6*A*). The *Af*FabI tetramerization domain links protomers along the *Q* axis interface and consists of an antiparallel four-helical bundle composed of interacting helices α4 (kinked) and α5 linking the A/C or B/D protomers (Fig. 6*B*). *Af*FabI α9–α9 interaction domain is a unique feature of clade 4 FabIs and links the A/D or B/C protomers along the *R* axis (Fig. 6*C*). Helix α9 extends from Ser-261 to Glu-275 and is amphipathic with the hydrophobic

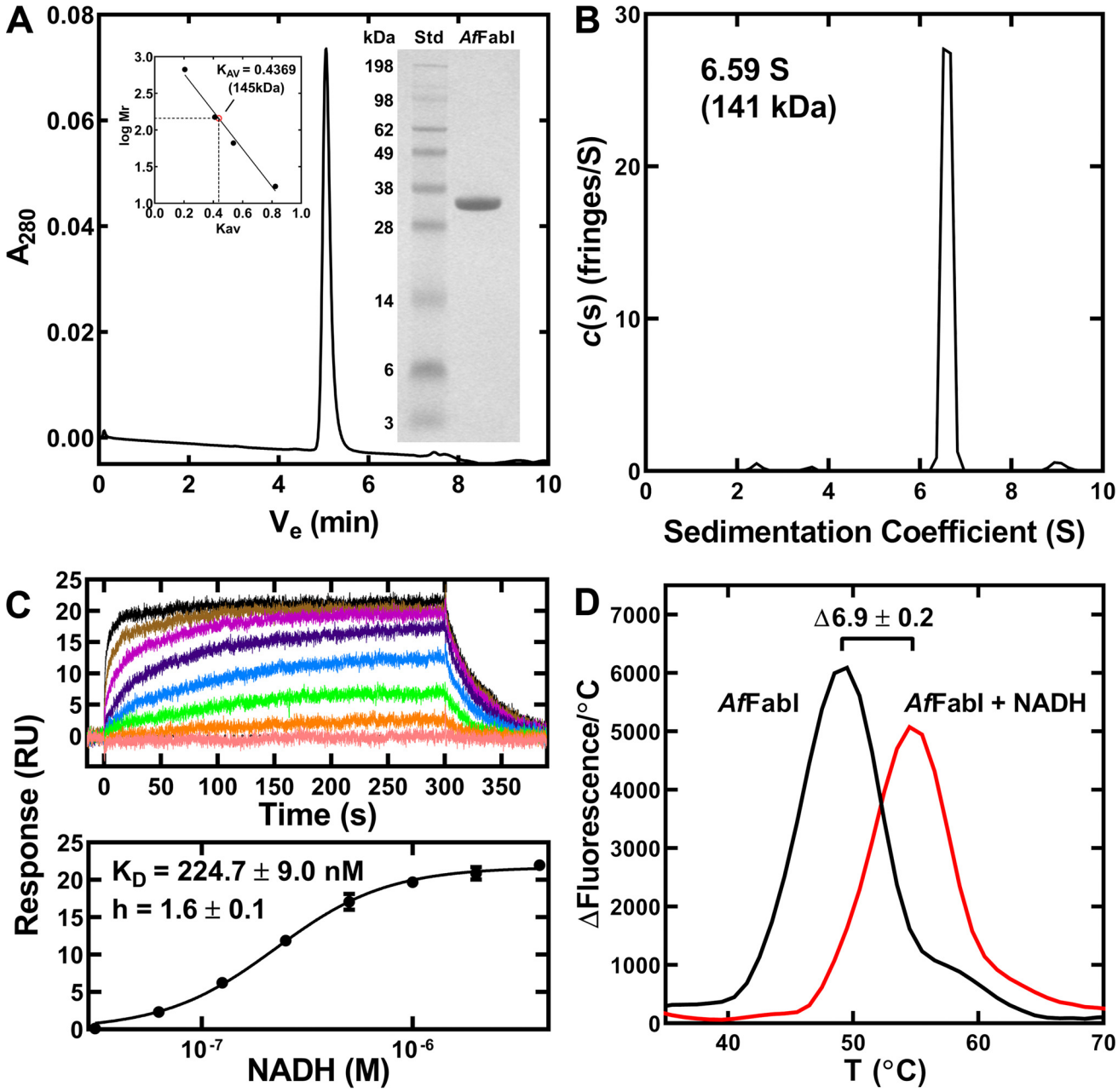

Figure 3. AfFabI oligomerization and NADH binding. *Af*FabI was purified by affinity and gel filtration chromatography. *A*, *Af*FabI migrated as a single 145 kDa species (V_e = 5.058 min) on a calibrated XBridge BEH SEC 200 Å 3.5-μm column (136 kDa theoretical mass). *Insets*, gel electrophoresis shows the purity of *Af*FabI (34 kDa) along with the indicated molecular weight standards (*Std*). The standard curve for the XBridge BEH SEC column used thyroglobulin (669 kDa), immunoglobin (150 kDa), BSA (66.4 kDa), and myoglobulin (17 kDa). *B*, the sedimentation velocity profiles (fringe displacement) were fitted to a continuous sedimentation coefficient distribution model *c*(*s*). *Af*FabI sedimented as a 141 kDa tetramer with a sedimentation coefficient of 6.59 S. *C*, surface plasmon resonance sensorgrams depicting one experiment to determine NADH binding to *Af*FabI (*top panel*). The data from three independent titrations were fit to the Hill equation using GraphPad Prism software to calculate the K_D and Hill coefficient (*h*). Mean ± S.E. (n = 3). *D*, protein thermal denaturation analysis was used to determine the stabilization of *Af*FabI by NADH. Assays contained 10 μM *Af*FabI (*black*) or 10 μM *Af*FabI + 100 μM NADH (*red*).

side chains forming the α9–α9 contact interface and the polar side chains extending into solvent.

The AfFabI·NADH binary complex

The 1.86 Å *Af*FabI·NADH complex structure was refined to R/R_{free} 15.8/19.7 (Table 1). The asymmetric unit contained one homotetramer. The protomers are nearly identical with a Cα RMSD of 0.13 Å across 282 residues and the NADH molecules were well-resolved in all four active sites. The planarity of the cofactor carboxamide relative to its attached pyridine ring is indicative of the NADH redox state (46). The C2N-C3N-C7N-O7N torsion angles in the NADH molecules were between 150.8° and 162.5° and are consistent with reduced NADH being present in the crystals. NADH binding increases the overall protomer surface area to ~15,000 Å^2, and the buried surface area of the subunit interfaces to ~5400 Å^2 (~36%). The active site lid containing α6 was not resolved in the *Af*FabI structure but was clearly seen in the *Af*FabI·NADH electron density map. The lid forms several hydrogen bond interactions with the pyrophosphate and nicotinamide of NADH (Fig. 7*A*). Nucleo-

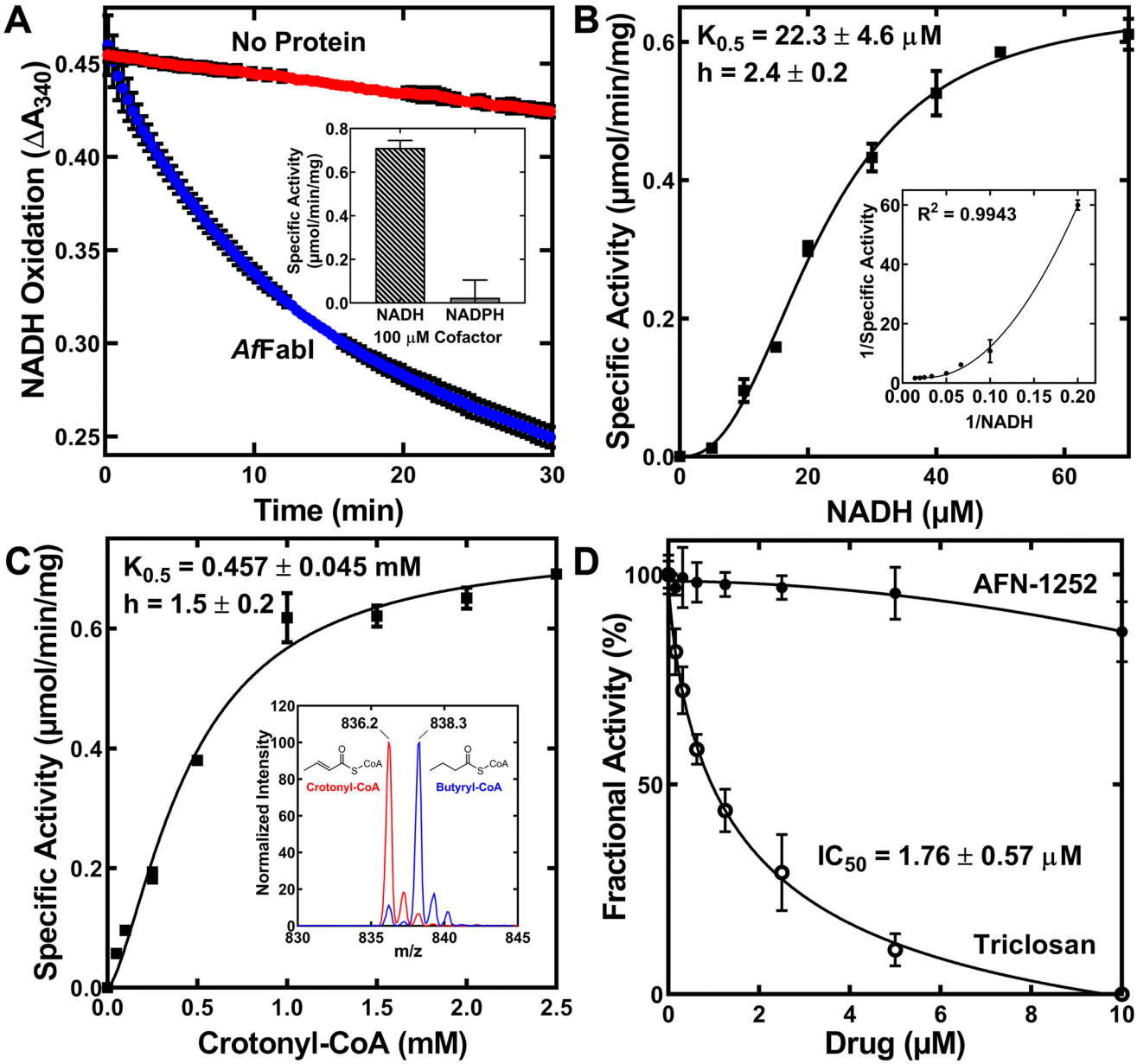

Figure 4. AfFabI displays prototypical FabI kinetics. *A*, the rate of 200 μM NADH oxidation in 1.25 mM crotonyl-CoA, 20 mM Tris-HCl, pH 8.0, as measured by the change in absorbance at 340 nm with (*blue*) or without (*red*) 100 nM *Af*FabI. The slope of the linear phase of the progress curve was converted to specific activity using the NADH extinction coefficient of 6220 M^{-1} cm^{-1}. *Inset*, NADPH did not support the reaction. *B*, specific activities were calculated as a function of NADH concentration. The behavior of *Af*FabI with NADH is best described by the Hill equation (*fitted line shown on graph*). *C*, specific activities were calculated as a function of crotonyl-CoA concentration. The behavior of *Af*FabI with crotonyl-CoA is best described by the Hill equation (*fitted line shown on graph*). *Inset*, mass spectrum analysis of the reaction mixture shows reduction of crotonyl-CoA (m/z = 836.2) to butyryl-CoA (m/z = 838.3) either with (*blue*) or without (*red*) *Af*FabI. *D*, fractional activity of *Af*FabI *versus* increasing concentrations of AFN-1252 or triclosan. Data points were fit to the inhibitor *versus* response. Variable slope nonlinear regression equation using GraphPad Prism 8.2.1 software and the fitted lines are shown on the graph. *Af*FabI spectrophotometric assays were performed in triplicate as described under "Experimental procedures." Mean ± S.E. (n = 3).

tide binding proteins often stabilize pyrophosphate binding using a positive helix dipole (47). Helix α1 creates this helix dipole in *Af*FabI and hydrogen bonds between NADH and lid residues Thr-199 side chain and Ala-201 backbone amide fix the cofactor in space. Lys-167 on α5 is part of the Tyr-Xaa$_6$-Lys catalytic dyad and donates two hydrogen bonds to the nicotinamide ribose to position and stabilize the nicotinamide (Fig. 7*A*). In addition, the nicotinamide moiety is also stabilized by hydrogen bonds that form between lid residue Thr-197 and the nicotinamide ring. The adenine moiety sits in a solvent-exposed hydrophobic pocket in the active site cavity. Hydrogen bonds between the adenine nitrogen N-1 and Ala-67 backbone carbonyl, and the adenine ribose and Asn-41 and Ser-45 side chains orient the adenine moiety in this cavity. The locations and interactions between *Af*FabI and NADH are very similar to other FabI proteins (48–51).

The NADH-induced conformational change creates four water-filled channels that connect the active sites to a central water well located in the core of the tetramer (Fig. 7*B*). These water channels enable efficient proton transfer to the active

Table 1
Data collection and model refinement statistics

PDB ID	*Af*FabI 6VLX	*Af*FabI·NADH 6VLY
Data collection		
Space group	$P2_122_1$	$P2_12_12_1$
Cell dimensions		
a, *b*, *c* (Å)	60.6, 77.8, 127.6	75.3, 111.5, 150.5
α, β, γ (°)	90, 90, 90	90, 90, 90
Resolution (Å)	35–1.72 (1.76–1.72)[a]	29–1.86 (1.91–1.86)
R_{merge}	0.056 (0.483)	0.077 (0.901)
$CC_{1/2}$	99.7 (90.9)	99.7 (77.0)
I/σ	13.4 (1.8)	12.6 (1.7)
Completeness (%)	98.3 (87.7)	94.4 (88.8)
Redundancy	6.4 (5.4)	4.9 (4.7)
Wilson B factor (Å^2)	25.8	24.7
Refinement		
Resolution (Å)	30–1.72 (1.76–1.72)	29–1.86 (1.91–1.86)
No. reflections	59,692 (3142)	100,112 (5169)
R_{work} (%)	20.6 (33.5)	15.8 (42.8)
R_{free} (%)[b]	24.5 (34.3)	19.7 (44.3)
Number of non-hydrogen atoms		
Protein	4110	8862
Ligand/ion	6	225
Water	402	1046
RMSD		
Bond lengths (Å)	0.006	0.010
Bond angles (°)	1.380	1.463
Average B factors (Å^2)	34.0	25.0
Ramachandran plot		
Favored (%)	95.4	96.8
Allowed (%)	4.4	3.0
Outliers (%)	0.2	0.2

[a] Statistics for the highest-resolution shell are shown in parentheses.
[b] R_{free} test set uses ~5% of the data.

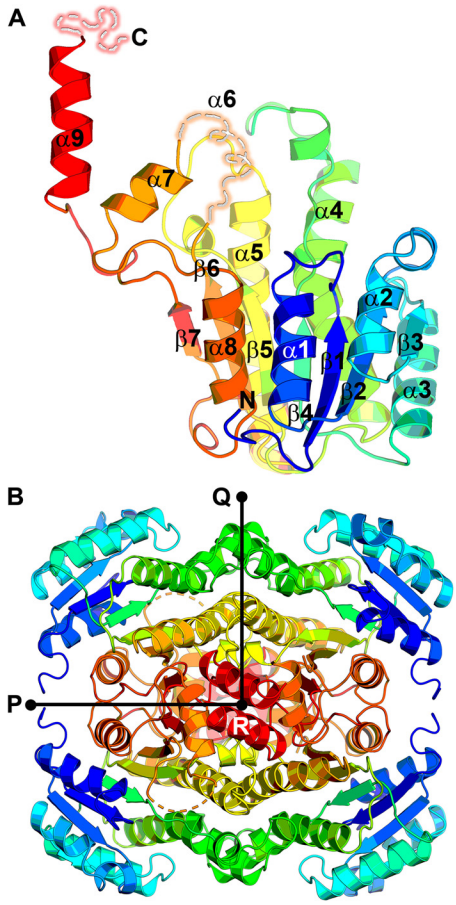

Figure 5. Overall crystal structure of *Af*FabI. *A*, the *Af*FabI monomer contains a Rossmann fold. The polypeptide chain is colored from *blue* (N terminus) to *red* (carboxyl terminus). The active site lid (α6) and terminal 13 residues are depicted as disordered (*broken dashes*) because these residues were not resolved in the electron density map. *B*, *Af*FabI is a tetramer with three perpendicular 2-fold noncrystallographic symmetry axes *P*, *Q*, and *R*.

sites for catalysis (52). The resolution of the *Af*FabI·NADH crystal structure enabled the visualization of ordered water molecules within the individual channels making hydrogen bond interactions with the peptide backbone (Fig. 7*C*). The individual water channels exit the active sites, narrow into tunnels that are formed by residues along the *R* axis of the promoter interfaces and empty into the water well at the center of the protein (Fig. 7*C*). The active site cavity is hydrated in the *Af*FabI crystal structure, and few ordered water molecules are detected because the water channels are only partially formed and the active site lid is open to solvent. As with other FabIs (52), the lid isolates the active site from bulk solvent to create an environment that promotes hydride transfer from NADH.

Helix α9 and the carboxyl terminus

A unique feature of *Af*FabI is how the clade 4–specific α9 helix and disordered carboxyl-terminal tail participate in the conformational change required for NADH binding (Fig. 8). In the example shown, helix $\alpha9^C$ and $\alpha9^B$ intertwine to connect the C/B partner protomers in *Af*FabI and the 13 residues of the protein attached to carboxyl terminus of α9 are disordered (Fig. 8*A*). In the *Af*FabI·NADH structure, the interacting α9 helices unwind, and along with 10 of the 13 disordered carboxyl-terminal amino acids (Val-277 to Glu-286), form an ordered loop feature that extends to the active site lid of the partner protomer (Fig. 8*B*). The N terminus of α7 lies at the base of the α9–α9 interaction domain and forms the corner of the active site cavity. The conformational change relocates the Cα chain of α9 up to 20 Å toward the opposite active site and drives the formation of a new protomer–protomer interaction interface that closes the active site and creates the water channels.

The active site is a large solvent-exposed crevice in the *Af*FabI structure (Fig. 9*A*). In this conformation, $Asn\text{-}213^C$ and $Asn\text{-}217^C$ from the last two turns of $\alpha7^C$ form hydrogen bonds with $Tyr\text{-}268^B$ from $\alpha9^B$. Upon NADH binding, the lid consisting of α6 and adjacent residues closes over NADH to convert the solvent-exposed crevice into an enclosed active site (Fig. 9*B*). $Asp\text{-}210^C$ from $\alpha7^C$ forms a hydrogen bond with $Thr\text{-}267^B$ from $\alpha9^B$ (Fig. 9*B*) as the unwound $\alpha9^B$ residues slide along $\alpha7^C$. Lid closure leaves the adenine moiety surface-exposed and buries the pyrophosphate and nicotinamide regions of NADH. The solvent-accessible surface area of the active site crevice decreases from ~500 Å^2 to ~300 Å^2. Every residue in the first turn of α9 in *Af*FabI forms a new hydrogen bond interaction in the *Af*FabI·NADH complex (Fig. 9*C*). The $Arg\text{-}262^B$ backbone amide nitrogen forms a hydrogen bond interaction with the $Tyr\text{-}179^A$ side chain from $\alpha5^A$ in the tetramerization domain. The $Arg\text{-}263^B$ side chain forms hydrogen bond interactions with backbone carbonyls from $Ser\text{-}219^B$, $Glu\text{-}216^B$, and $Asn\text{-}217^B$ from $\alpha7^B$ in the corner of the protomer B active site. The $Ala\text{-}264^B$ backbone amide forms a hydrogen bond interaction with the $Ser\text{-}261^B$ side chain at the base of $\alpha9^B$, and the backbone carbonyls from $Arg\text{-}263^B$ and $Met\text{-}265^B$ form hydrogen bond interactions with the $Lys\text{-}266^C$ side chain from $\alpha9^C$. Two

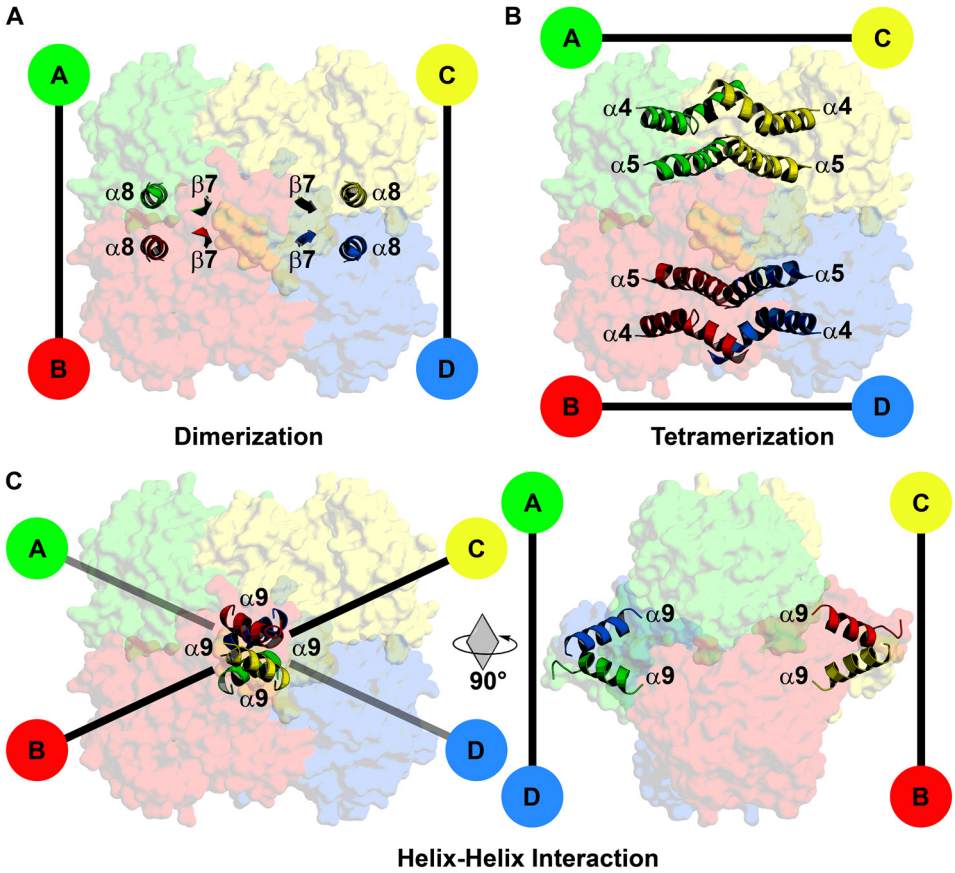

Figure 6. Subunit interface domains of *Af*FabI. Specific structural domains link the protomers along the *P*, *Q*, and *R* axes interfaces. *A*, the dimerization domain consists of interacting α8 helices and β7 strands that link protomers A/B and C/D along the *P* axis. *B*, the tetramerization domain is an antiparallel four-helix bundle composed of α4 and α5 that links protomers A/C and B/D along the *Q* axis. *C*, the carboxyl-terminal α9 helix–helix interaction domain is a unique feature of *Af*FabI. This domain links protomers A/D and B/C along the *R* axis. Rotation of the tetramer by 90° around the *Q* axis enables clear visualization of the protomer–protomer interaction mediated by α9.

residues in the second turn of α9 form new hydrogen bond interactions in *Af*FabI·NADH. In addition to the Thr-267^{B}–Asp-210^{C} interaction shown in Fig. 9*B*, the side chain of Lys-266^{B} forms hydrogen bonds with Arg-263^{C} and Met-265^{C} from α9^{C} (Fig. 9*D*). There are no protein–protein interactions formed between the loop residues derived from the third turn of α9 in *Af*FabI and the protomers in the *Af*FabI·NADH structure. This loop extends away from the surface as seen in Fig. 8*B*.

Ten carboxyl-terminal–disordered residues after α9^{B} in the *Af*FabI structure become ordered to create a channel connecting the active site to the water well in the *Af*FabI·NADH structure (Fig. 9*E*). These interactions form "latches" along the *R* axis that create the surface enclosing a water channel. The first latch is formed by Glu-275^{B} backbone amide, and Asp-276^{B} side chain hydrogen bonds to Arg-183^{A} and Tyr-158^{C} side chains (Fig. 9*E*). Asp-276^{B} is oriented to coordinate a water molecule in the channel. Arg-262^{B} in the first turn of α9^{B} forms a planar stacking interaction (53) between the guanidinium group in the side chain and the aromatic ring of Tyr-158^{C}. A van der Waals contact distance is formed between lid residue Leu-206^{C} side chain and Glu-275^{B} backbone carbonyl. The second latch is formed by His-278^{B} backbone amide hydrogen bonding to the Thr-106^{C} and Asp-108^{C} side chains, and Gln-279^{B} backbone carbonyl and side chain hydrogen bonds to the Arg-134^{A} backbone carbonyl and side chain (Fig. 9*E*). A van der Waals contact is formed between the Val-277^{C} and Ile-180^{A} side chains (not shown in Fig. 9). The molecular latches convert a region of the tetramer that freely exchanges with bulk solvent in *Af*FabI into an enclosed channel that connects the active site with the central water well in *Af*FabI·NADH. These data indicate that the conformational changes associated with α9 and the carboxyl terminus are important for catalysis because they participate in the formation of the catalytic center and the water channel that connects the active site to the water well.

Function of the carboxyl terminus

We constructed a series of truncation mutants to test the role of α9 and the disordered carboxyl terminus in catalysis. All the truncated mutant enzymes had similar turnover numbers ($V_{max}/[E_T]$) but had reduced catalytic efficiencies ($V_{max}/[E_T]/K_{0.5}$) that were driven by defects in the apparent $K_{0.5}$ for NADH (Table 2). *Af*FabI(1–273) lacked the disordered carboxyl-terminal residues in the *Af*FabI structure and eliminated the interactions contributing to sealing the water channels in the *Af*FabI·NADH structure illustrated in Fig. 9*E*. *Af*FabI(1–273) was a tetramer that was stabilized by NADH, but the catalytic efficiency of the enzyme was reduced by 3-fold driven by an increase in the apparent $K_{0.5}$ for NADH (Table 2). Although *Af*FabI(1–273) was catalytically compromised, it was able to complement the growth of the *fabI*(Ts) mutant when overex-

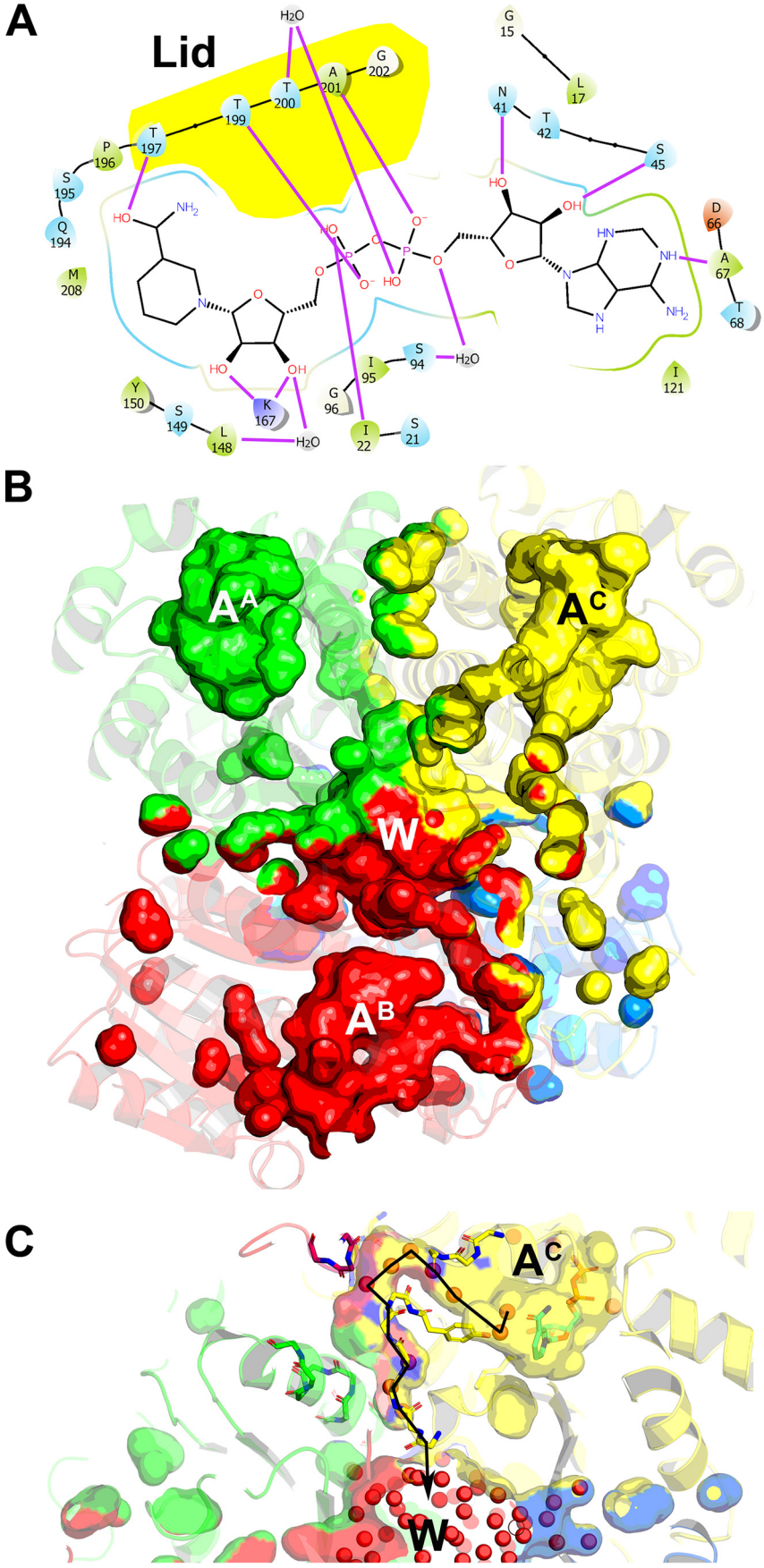
A
Lid
B
W
C
W

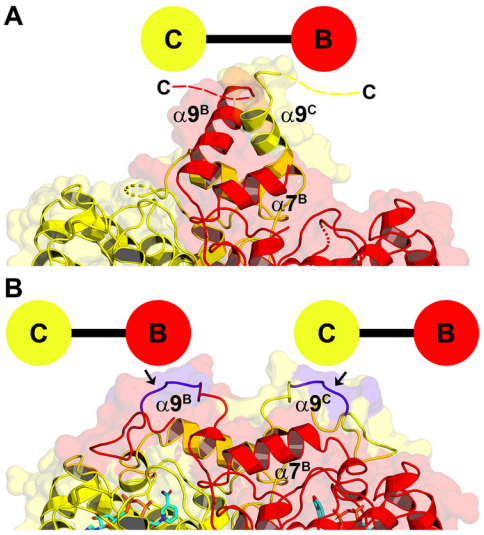

Figure 8. Conformational change in helix α9 and the carboxyl terminus. *A*, in the *Af*FabI crystal structure, the $\alpha9^C$ and $\alpha9^B$ helices are wound together, connecting the C and B protomers, and the last 13 residues of the protein are disordered. *Broken dashes* indicate the relative location of missing carboxyl terminus residues. *B*, in the *Af*FabI·NADH crystal structure, the $\alpha9^C$–$\alpha9^B$ interaction domain unwinds, and 10 of the 13 carboxyl-terminal residues form a structured loop feature that connects to the active site lid of the partner protomer. The *arrows* denote the location of residues (*purple*) in the α9 turn that are removed in the *Af*FabI(1–269) truncation mutant.

pressed. *Af*FabI(1–269) removed four resides (1 turn) from α9 in the *Af*FabI structure. This region did not form any specific protein contacts in the *Af*FabI·NADH structure because it loops away from the protein and the side chains point toward solvent (Fig. 8*B*, *arrows*). Thus, the biochemical properties of *Af*FabI(1–269) were similar to the properties of *Af*FabI(1–273). The *Af*FabI(1–265) truncation removed the second turn of the α9 helix and the important interactions depicted in Fig. 9, *B* and *D*. These two interactions are key to closing one side of the lid that lays over the active site in the *Af*FabI·NADH structure and would be predicted to compromise NADH binding. *Af*FabI(1–265) was a thermally stable tetramer but was not stabilized by the addition of NADH (Table 2). The apparent $K_{0.5}$ for NADH increased 6-fold and the catalytic efficiency dropped by 5.5-fold leading to a protein that could not complement the *fabI*(Ts) mutant even when overexpressed (Table 2). *Af*FabI(1–261) removed the remaining turn of the α9 helix and the multiple interactions depicted in Fig. 9*C*. These interactions connect protomers A and C with protomer B and form a junction with the NADH lid. *Af*FabI(1–261) reduces *Af*FabI to the clade 1 structure. Like clade 1 enzymes it is stable and cooperative but had a 23-fold increase in the NADH apparent $K_{0.5}$ and was 22.5-fold less catalytically efficient (Table 2). These data show the importance of α9 and the carboxyl terminus in creating the substrate binding lid and the water channels required for efficient catalysis.

Discussion

This work defines the function of the structural features that are unique to clade 4 FabIs. The four clades of bacterial FabIs diverged from their common ancestor in the distant past and each have a long and unique evolutionary history. All FabIs have common features like a Rossmann fold, cofactor-induced conformational change, Tyr-*X*aa$_6$-Lys catalytic dyad, and dimerization and tetramerization interfaces. These basic structural features are embodied in the prototypical clade 1 *Ec*FabI structure depicted in Fig. 10, *upper panel*. Using the clade 1 enzymes as the prototypical comparator, each of the other three clades possesses a unique structural feature. Clade 2 FabIs are the *Mycobacterium* InhA enzymes that have a deeper active site crevice and longer α6 lid than the other FabI clades. These features are thought to enable InhA to bind very long– chain enoyl-ACP substrates for the synthesis of cell wall mycolic acids (28, 54). Clade 3 FabIs have an insertion between β3 and α3 that creates peripheral loops that are related by the *Q* axis interface. A functional or structural role is yet to be described for this feature in the plastid FabIs. Clade 4 FabIs have an extension of the carboxyl terminus that provides a new protomer–protomer interaction surface that links protomers along the *R* axis. This study shows that the carboxyl-terminal extension is critical for catalysis in clade 4 FabIs by participating in the conformational change that creates the NADH-binding pockets and water channels that feed the active site. This unique feature is present in all the Bacteroidetes FabIs and has evolved into a domain that is essential for catalysis in clade 4 enzymes.

Further, our data explain why a potent antimicrobial drug that targets the FabI of clade 1 and three pathogens does not impact a major constituent of the microbiome. AFN-1252 is a *S. aureus*–selective (Fig. 10, *lower panel*) FabI inhibitor that was developed as a pathogen-specific drug (16, 17). Treatment of mice with AFN-1252 does not perturb the Bacteroidetes phylum in the gut microbiome, whereas broad-spectrum antibiotics devastate the microbiome (24). Bioinformatic analysis of the microbiome enoyl-ACP reductase distribution indicates the presence of FabK in the Clostridia and commensal Bacteroidetes, and the expression of FabK would account for the resistance of organisms to AFN-1252. However, many Bacteroidetes genera only express a FabI (Fig. 1*B*). Biochemical analysis shows that clade 4 FabIs are resistant to AFN-1252, explaining why Bacteroidetes genera are not impacted by AFN-1252 therapy. AFN-1252 is a rigid small molecule that contains

Figure 7. Active site and water channels in the *Af*FabI·NADH complex upon NADH binding. *A*, schematic diagram shows hydrogen bond interactions between the active site and NADH designated by *purple lines*. Lid residues that interact with NADH are shown by *yellow highlight*. *B*, molecular surface rendering of the central water well that connects to the four active sites was visualized in the *Af*FabI·NADH complex crystal structure along with the water channels that connect each active site with the water well using PyMOL. The molecular surface of the water channels and central water well are colored according to the contribution from each protomer. Segments of each water channel have more than one color because they are formed by the protomer interfaces along the *R* axis. The active sites in each protomer are designated with the letter *A* and the protomer superscript, and the letter *W* indicates the location of the central water well. *C*, each water channel contains ordered water molecules (*red spheres*) that form hydrogen bond interactions with each other and the peptide backbone. The *line* traces the chain of structured waters that begin at the carboxyamide of NADH in the active site (A^C), exit into a narrow tunnel formed by the A/B/C protomer interfaces along the *R* axis, and empty into the central water well (*W*).

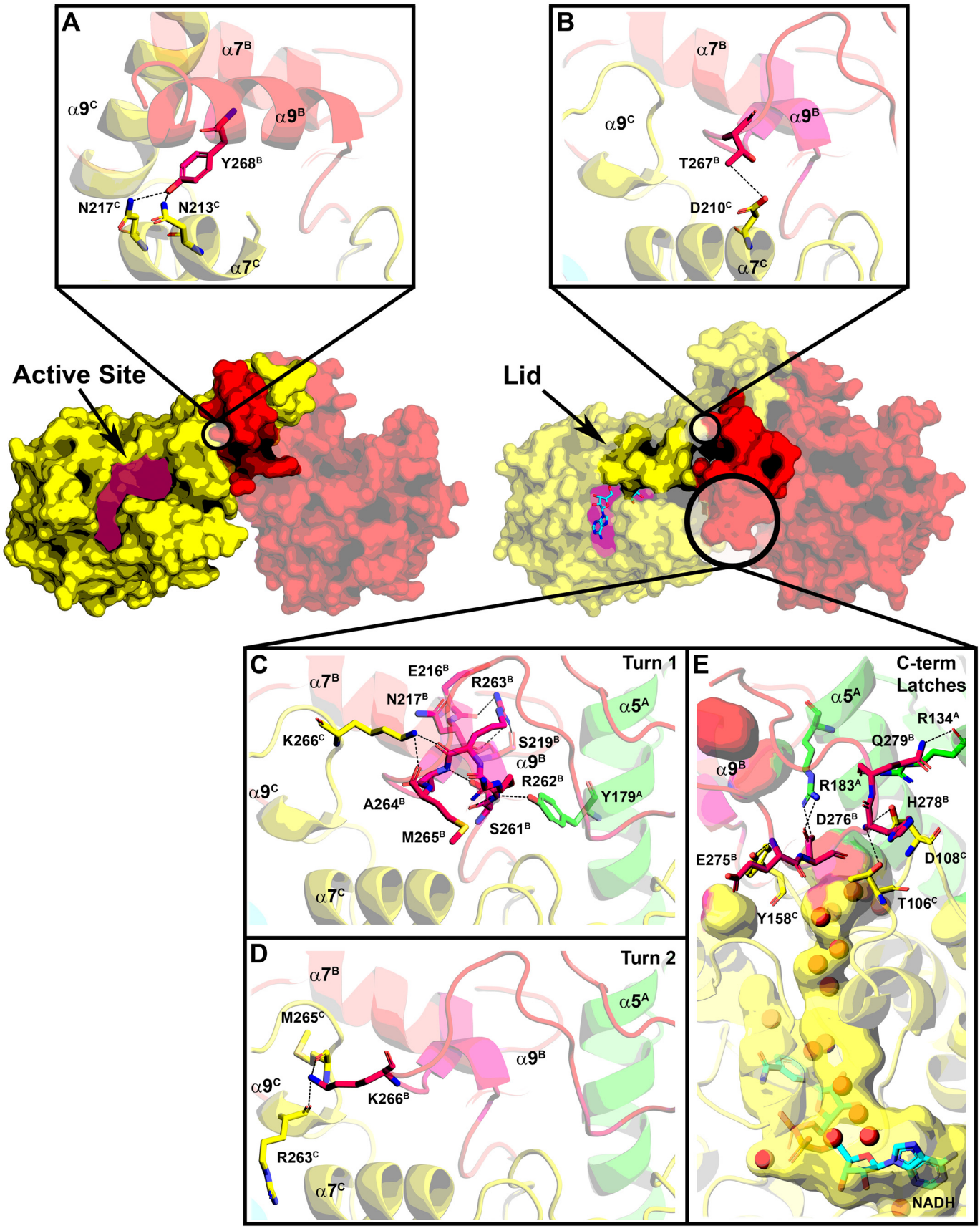
A
α7B
α9C
α9B
Y268B
N217C
N213C
α7C
B
α7B
α9C
α9B
T267B
D210C
α7C
Active Site
Lid
C
Turn 1
α7B
E216B
R263B
N217B
α5A
K266C
S219B
α9B
R262B
α9C
A264B
Y179A
M265B
S261B
α7C
D
Turn 2
α7B
α5A
M265C
α9B
α9C
K266B
R263C
α7C
E
C-term Latches
α5A
R134A
Q279B
α9B
R183A
H278B
D276B
E275B
D108C
T106C
Y158C
NADH

Table 2
Properties of *Af*FabI carboxyl-terminal truncation mutants

Property	*Af*FabI[a](1–289)	*Af*FabI(1–273)	*Af*FabI(1–269)	*Af*FabI(1–265)	*Af*FabI(1–261)
Complementation					
fabI(Ts)	Yes	Yes	Yes	No	No
Biophysical properties					
s_{20}	6.59	6.40	6.37	6.18	6.11
Thermal stability					
Ligand-free (°C)	47.9 ± 0.1	46.0 ± 0.2	45.0 ± 0.1	48.8 ± 0.2	52.1 ± 0.4
+ NADH (°C)	54.8 ± 0.2	52.1 ± 0.2	50.5 ± 0.3	49.3 ± 0.2	51.4 ± 0.2
ΔT (°C)	6.9 ± 0.2	6.1 ± 0.3	5.5 ± 0.4	0.5 ± 0.4	−0.7 ± 0.6
Biochemical properties					
NADH $K_{0.5}$ (μM)	52.8 ± 3.0	160.3 ± 22.2	127.1 ± 10.9	291.9 ± 31.8	1225.0 ± 47.5
h^b	2.1 ± 0.2	1.4 ± 0.2	1.3 ± 0.1	1.0 ± 0.1	2.6 ± 0.2
$V_{max}/[E_T]^c$ (min^{-1})	6.45 ± 0.19	6.57 ± 0.24	7.26 ± 0.19	6.46 ± 0.21	6.63 ± 0.18
$V_{max}/[E_T]/K_{0.5}{}^d$ (10^{-3} μmol^{-1} min^{-1})	122.12 ± 3.64	40.97 ± 1.51	57.13 ± 1.52	22.14 ± 0.71	5.41 ± 0.15

[a] *Af*FabI(1–289) is the full-length, wildtype protein.
[b] Hill number.
[c] Turnover number. $[E_T]$ = total enzyme concentration.
[d] A measure of catalytic efficiency.

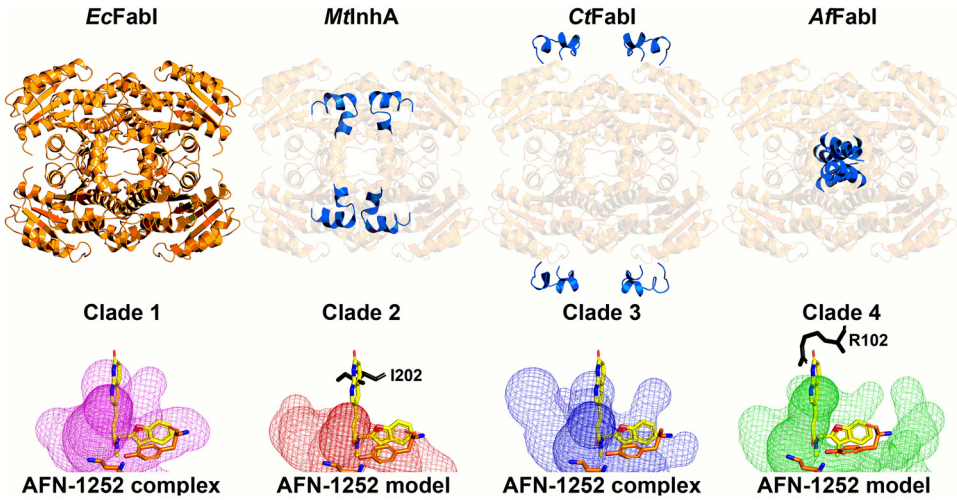

Figure 10. Unique structural features of the FabI clades. Representative models for the four FabI clades are compared using clade 1 FabI as the standard for comparison. *Top panel*, clade 1 *Ec*FabI has the basic Rossmann fold and tetrameric organization common to all FabIs. The unique features in clades 2–4 are highlighted in *blue*. Clade 2 enzymes are represented by the Mycobacterial enoyl-ACP reductase (*Mt*InhA). Clade 2 enzymes contain an extended active site lid to accommodate the long acyl-ACP substrates (28 carbons) that arise during the synthesis of mycolic acids. Clade 3 plastid enzymes are represented by the Chlamydial *Ct*FabI and contain peripheral loops of unknown function. Clade 4 enzymes are presented by *Af*FabI and contain carboxyl-terminal α9–α9 coiled coils that are required for high-affinity NADH binding. *Bottom panel*, active site volumes for each clade are depicted by a surface mesh. The catalytic lysine and tyrosine residues are shown in *orange*. Ternary complex structures of clade 1 (PDB ID: 4JQC) (77) and 3 (PDB ID: 4Q9N) (29, 83) enzymes with NAD(H) and AFN-1252 (shown in *yellow*) have been determined and contain active site volumes that bind AFN-1252. Binary complex structure of clades 2 (PDB ID: 4DRE) (78, 82) and 4 (PDB ID: 6VLY) enzymes with NAD(H) have been determined, and AFN-1252 was modeled in their active site volumes with respect to the tyrosine. In both cases, the 3-methylbenzofuran moiety of AFN-1252 extends outside the active site and the oxotetrahydronaphthyridine moiety clashes with amino acid residues (shown in *black*).

an oxotetrahydronaphthyridine and 3-methylbenzofuran moiety connected by a *cis*-amide. All three components of the drug form interactions with the protein in AFN-1252–sensitive FabIs in clades 1 and 3 (19, 29). The *Af*FabI·NADH crystal structure shows that clade 4 FabIs have a differently shaped active site cavity than clade 1 and 3 enzymes (Fig 10, *lower panel*). In *Af*FabI, the lid residue Val-205 side chain occupies the space where the 3-methylbenzofuran moiety should reside and the Arg-102 side chain sterically clashes with the oxotetrahydronaphthyridine moiety. Similarly, modeling AFN-1252 in the clade 2 active site reveals a steric clash with Ile-202. These considerations suggest that FabI-targeted drugs against clade 1 or 3 pathogens would have the benefit of having little to no impact on the gut microbiome, sparing patients the complications that arise from current therapies that destroy the microbiome (55, 56).

Figure 9. Creation of the NADH-binding site. The active site lid is disordered in the absence of NADH and helix $\alpha9^B$ (*red*) is coiled around $\alpha9^C$ (*yellow*) along the *R* axis. NADH (*cyan*) binding to the active-site crevice orders the lid. *A*, Tyr-268[B] in the second turn of helix α9 in the *Af*FabI structure forms hydrogen bond interactions with Asn-217[C] and Asn-213[C] in the second two turns of $\alpha7^C$. *B*, following NADH binding, the unwound $\alpha9^B$ slips along $\alpha7^C$. The Thr-267[B] side chain on $\alpha9^B$ forms a hydrogen bond interaction with Asp-210[C] in the first turn of $\alpha7^C$. *C*, residues in the first turn of α9 in the *Af*FabI structure become an ordered loop in *Af*FabI·NADH with multiple hydrogen bond interactions with the other protomer. *D*, Lys-266[B] from the second turn of α9 in *Af*FabI form hydrogen bond interactions with Arg-263[C] and Met-265[C] from $\alpha9^C$ in *Af*FabI·NADH. *E*, hydrogen bond interactions between the disordered carboxyl terminus of *Af*FabI with the other protomers in *Af*FabI·NADH. The backbone amine of Glu-275[B] forms a hydrogen bond with the Tyr-158[C] side chain, the side chain of Asp-276[B] forms a hydrogen bonds to the side chain of Arg-183[A] (on $\alpha4^A$), the backbone amine of His-278[B] forms a hydrogen bond interaction with the Thr-106[C] and Asp-108[C] side chains and the backbone carbonyl and side chain from Gln-279[B] forms hydrogen bonds with the side chain and backbone carbonyl of Arg-134[A] from $\alpha5^A$.

Table 3
Bacterial strains and plasmids

	Description	Reference
Strain		
E. coli JP1111	Hfr(PO1), *galE45*(GalS), λ^-, *fabI392*(Ts), *relA1*, *spoT1*, *thiE1*	79
E. coli ANS1	*metB1 relA1 spoT1 gyrA216 tolC::Tn10* λ^- λ^r F^-	63
Plasmid		
pPJ131	*E. coli* expression vector	80
p*Ec*FabI	*E. coli fabI* in pPJ131	29
p*Ct*FabI	*Chlamydia trachomatis fabI* in pPJ131	29
p*Af*FabI	*A. finegoldii fabI* (UniProt ID: A0A174E195) in pPJ131	This study
p*Ca*FabK	*Clostridium acetobutylicum fabK* in pPJ131	37
p*Af*FabK	*A. finegoldii fabK* (UniProt ID: I3YI65) in pPJ131	This study
pET_*Af*FabI	*A. finegoldii fabI 1–289* (UniProt ID: A0A174E195) in pET28b	This study
pET_1–273	*A. finegoldii fabI 1–273* (UniProt ID: A0A174E195) in pET28b	This study
pET_1–269	*A. finegoldii fabI 1–269* (UniProt ID: A0A174E195) in pET28b	This study
pET_1–265	*A. finegoldii fabI 1–265* (UniProt ID: A0A174E195) in pET28b	This study
pET_1–261	*A. finegoldii fabI 1–261* (UniProt ID: A0A174E195) in pET28b	This study

Experimental procedures

Materials

All chemicals and reagents were obtained from Sigma-Aldrich or Fisher unless otherwise indicated. Strains and plasmids used in this work are listed in Table 3.

Phylogeny

Predicted FabI sequences were collected from the NCBI Reference Sequence database to include characterized FabI sequences and their homologs. Maximum likelihood phylogenetic trees were constructed using the DECIPHER and phangorn packages in R (57, 58). Briefly, sequences were aligned using the AlignSeqs and StaggerAlignment functions in DECIPHER. The LG + Γ (4) + I model (59) was best fitting by the Bayesian information criteria from the model. Test function in phangorn evaluating the WAG, JTT, LG, and Dayhoff amino acid replacement matrix models with and without gamma distributed rate variation among sites (Γ) and invariant sites (I). The initial neighbor-joining tree was constructed using the distance matrix, with the maximum likelihood tree generated from the neighbor-joining tree using the LG + Γ (4) + I model with stochastic branch rearrangement. Bootstrap method of 1000 replicate trees was used to determine the confidence of the tree topology. The maximum likelihood tree was visualized using ggtree (60).

Molecular biology

The predicted *A. finegoldii* FabI and FabK have been previously identified (61). Representative predicted *A. finegoldii* genes *AffabI* (UniProt ID: A0A174E195) and *AffabK* (UniProt ID: I3YI65) were optimized for gene expression in *E. coli* using GeneArt Gene Synthesis Technology (Life Technologies). An NdeI restriction site was engineered at the 5′-end of the gene with the start codon in the NdeI site, whereas a stop codon and an EcoRI restriction site were sequentially engineered at the 3′-end of the gene. The genes were cloned into the pPJ131 plasmid (a modified version of the pBluescript plasmid with the multiple cloning site from pET28a) via the NdeI and EcoRI (New England Biolabs) restriction sites (29, 80). To create the *AffabI* carboxyl-terminal truncation mutant constructs, premature stop codons were engineered into the gene using the QuikChange II Site-Directed Mutagenesis Kit (Agilent) and primers 5′-CAAGCATGGGTATGTCA**TGATGA**CGTCGTGCAATGAAAAC, 5′-TGTCACGTCGTGCAATG**TGATGA**AAAAACCTATGAAAAAGG, 5′-CAATGAAAACCTATGAA**TGATGA**AAAGGTATGCGCTTTGA, and 5′-ATGAAAAAGGTATGCGC**TGATGA**TTTGAAGATGTGCACCA and their reverse complements (The bold letters emphasize the stop codons that were engineered into the gene sequence). The amino acid numbering convention used assumes the initiating methionine of the native protein as residue 1. For protein purification, the *AffabI* constructs were cloned into the pET28b plasmid via the NcoI and EcoRI (New England Biolabs) restriction sites.

Complementation assay

The *Af*FabK amino acid sequence contains an FMN-binding motif (5); the *Af*FabI does not. The *trans*-2-enoyl–ACP reductase function of *Af*FabI and *Af*FabK was confirmed using the previously established complementation method (3, 29). Expression plasmids were constructed to overexpress nothing (negative control), *E. coli* FabI (*Ec*FabI), *C. trachomatis* FabI (*Ct*FabI), *Af*FabI and its truncation mutants, *C. acetobutylicum* FabK (*Ca*FabK) (37), or *A. finegoldii* FabK (*Af*FabK) and then transformed into *E. coli* strain JP1111 (*fabI*(Ts)) (79) and plated at 30 °C on LB plates containing 100 μg/ml carbenicillin. Individual colonies were streaked on plates containing 100 μg/ml carbenicillin and incubated at 30 °C and 42 °C. Carbenicillin stress slows growth at 42 °C. Strain JP1111 is nonviable at 42 °C unless complemented with a functional *trans*-2-enoyl–ACP reductase, such as *Ec*FabI or *Ca*FabK that serve as positive controls.

Minimum inhibitory concentration analysis

The minimum inhibitory concentrations for AFN-1252 and triclosan against *E. coli* strain ANS1 (Δ*tolC*) were determined using a broth microdilution method as described previously (62). ANS1 is a *tolC* knockout mutant that is used to eliminate the contribution of type 1 secretion systems to drug resistance (63). Briefly, pPJ131 expression plasmids containing nothing, *Ec*FabI, *Ct*FabI, *Af*FabI, *Ca*FabK, or *Af*FabK were transformed into ANS1, and these strains were grown to A_{600} = 0.6 in LB before being backdiluted 1:30,000 in 1% DMSO in 1% tryptone media. Diluted cells (100 μl) were added to each well of a U-bot-

tom 96-well plate except the first column of wells. Diluted cells (200 μl) were mixed with 50 μM AFN-1252 or 50 μM triclosan was added to the first column of wells, and 100 μl was serially diluted through the plate excluding the last column of wells, leaving 100 μl of cells in each well with the appropriate concentration of compound. The plate was incubated at 37 °C for 24 h and then read at 600 nm using a SPECTRAmax 340PC Microplate Reader. Cells from each strain grown with 0 μM compound were used as a reference (*i.e.* 100% fractional growth).

AfFabI protein expression and purification

BL21 (DE3) cells harboring the pET-*Af*FabI plasmid were grown in LB medium with 100 μg/ml carbenicillin at 37 °C and 200 rpm shaking to $A_{600} = 0.6$. The culture was cooled to 16 °C then induced with 1 mM isopropyl 1-thio-β-D-galactopyranoside overnight. Cells were centrifuged and pellets were resuspended in 20 mM Tris-HCl, pH 8.0, 200 mM NaCl, 10 mM imidazole (30 ml/liter culture). Cells were lysed via a cell disruptor and the amino-terminal His_6-tagged *Af*FabI was purified by standard nickel chelation chromatography (29). The protein was then gel filtered into 20 mM Tris-HCl, pH 8.0, 200 mM NaCl, 10 mM EDTA using a preparative Superdex 200 column with dimensions 16 mm × 60 cm. The *Af*FabI molecular weight was estimated using an analytical XBridge BEH SEC 200 Å 3.5-μm column with dimensions 7.8 mm × 150 mm. Approximately 26 mg of purified *Af*FabI was obtained per liter of culture. The same methods were used to overexpress and purify *Af*FabI mutant proteins.

Analytical ultracentrifugation

Sedimentation velocity experiments were conducted in a ProteomeLab XL-I analytical ultracentrifuge (Beckman Coulter) following standard protocols unless mentioned otherwise (64, 65). Samples in buffer containing 20 mM Tris-HCl, pH 8, 200 mM NaCl, 10 mM EDTA were loaded into cell assemblies comprised of double sector charcoal-filled centerpieces with a 12 mm path length and sapphire windows. The cell assemblies, containing identical sample and reference buffer volumes of 390 μl, were placed in a rotor and the samples and cells were incubated at 20 °C for 2 h before being accelerated from 0 to 50,000 rpm. Rayleigh interference optical data as well as absorbance data at 280 nm were collected at 1-min intervals for 12 h. The velocity data were modeled with diffusion-deconvoluted sedimentation coefficient distributions c(s) in SEDFIT (RRID: SCR_018365) using algebraic noise decomposition and with signal-average frictional ratio and meniscus position refined with nonlinear regression (66). The s-value was corrected for time and finite acceleration of the rotor was accounted for in the evaluation of Lamm equation solutions (67). Maximum entropy regularization was applied at a confidence level of $p = 0.68$. The partial specific volumes of the proteins, based on its amino acid composition, was calculated in SEDFIT.

Enzymology

The *Af*FabI enzymatic activity was determined by measuring the conversion of NADH to NAD^+ at 340 nm. The enzyme reactions were 100 μl in volume and monitored in Costar UV half-area 96-well plates with a SPECTRAmax 340PC instrument taking 340-nm readings at 10-s intervals at 30 °C. In these experiments, enzyme concentrations are reported relative to monomer concentration. The velocity of the *Af*FabI enzyme (100 nM) was measured by adding 1.25 mM crotonyl-CoA and 100 μM NADH in 20 mM Tris-HCl, pH 8.0. The apparent $K_{0.5}$ of crotonyl-CoA was determined by adding 100 nM *Af*FabI to 200 μM NADH and 0, 0.05, 0.1, 0.25, 0.5, 1, 1.5, 2, or 2.5 mM crotonyl-CoA. The apparent $K_{0.5}$ of NADH was determined by adding 100 nM *Af*FabI to 1.25 mM crotonyl-CoA and 0, 5, 10, 15, 20, 30, 40, 50, or 70 μM NADH. The reactions were mixed for 10 s by the mix function on the plate reader, and data were acquired at 10-s intervals for 30 min. Initial velocity was calculated from the linear phase of the progress curve and fit using the Hill equation to determine the apparent $K_{0.5}$ (68). The IC_{50} of AFN-1252 and triclosan were measured above saturating substrate concentrations (100 nM *Af*FabI, 1.25 mM crotonyl-CoA, and 200 μM NADH in 20 mM Tris-HCl, pH 8.0) against 0, 0.15, 0.31, 0.62, 1.25, 2.5, 5, and 10 μM compound. Initial velocities comparing *Af*FabI full-length and truncated proteins were determined using a Waters e2695 Separations Module HPLC system. Protein (100 nM) was added to 1.25 mM crotonyl-CoA and 0, 5, 10, 15, 20, 30, 40, 50, 60, 125, 250, 500, 1000, 2000, 4000 μM NADH in 20 mM Tris-HCl, pH 8.0. The enzyme reactions were 40 μl in volume and incubated for 10 min at 30 °C. Reactions were stopped by adding equal volume methanol and applied to a Gemini C18, 3 μm 100 Å, 4.6 mm × 150 mm column at a 0.5 ml/min flow rate. Butyryl-CoA product was separated from crotonyl-CoA substrate by gradient elution and monitored at A_{260}. The 30-min gradient was from 90% 50 mM KH_2PO_4, pH 4.6, acetonitrile (90/10, v/v) to 40% 50 mM KH_2PO_4, pH 4.6, acetonitrile (40/60, v/v). All kinetic experiments were run in triplicate.

Surface plasmon resonance experiments

Surface plasmon resonance experiments were conducted at 20 °C using a ForteBio Pioneer optical biosensor (ForteBio). Poly–His-tagged *Af*FabI constructs were immobilized on polycarboxylate hydrogel-coated gold chips preimmobilized with nitrilotriacetic acid (HisCap chips, ForteBio). The chip was primed in chelating buffer (10 mM HEPES, pH 7.4, 150 mM NaCl, 50 μM EDTA, 0.005% Tween 20) and was preconditioned at 10 μl/min with three 60-s injections of wash buffer (10 mM HEPES, pH 8.3, 150 mM NaCl, 350 mM EDTA, 0.05% Tween 20) and one 60-s injection of chelating buffer before being charged with a 60-s injection of 500 μM $NiCl_2$ in chelating buffer. After priming into binding buffer (20 mM Tris-HCl, pH 8.0, 200 mM NaCl, 0.01% Brij-35, 5% DMSO), FabIs were injected until ~1500–1700 resonance units of protein were captured. One flow cell on the chip was charged with Ni^{2+} without adding protein to be used as a reference cell.

NADH was prepared in binding buffer as a 2-fold dilution series with maximum concentration of 4 μM for binding to *Af*FabI and was injected in triplicate for each concentration at a flow rate of 30 μl/min. A series of buffer-only (blank) injections was included throughout the experiment to account for instrumental noise. NADH fully dissociated from the protein surfaces, eliminating the need for a regeneration step. The data were processed, double-referenced, microcalibrated, and ana-

lyzed using the software package Qdat (version 4.3.1.2, ForteBio). Equilibrium binding levels were determined and exported to GraphPad Prism for fitting to the Hill equation.

Protein thermal shift assays

Protein thermal shift analysis was conducted to investigate if NADH enhanced the thermal stability of the *Af*FabI constructs. Solutions (30 μl) of *Af*FabI (10 μM) and *Af*FabI (10 μM) + NADH (100 μM) in 20 μM HEPES, pH 7.5, 150 mM NaCl, 20 mM $MgCl_2$, and 2.5× Sypro Orange Dye were added to wells of ThermoGrid optically clear PCR plates (Denville Scientific). The plates were centrifuged at 1000 × *g* for 5 min and then analyzed by the ABI 7300 real-time PCR system as described previously (29). The temperature was ramped from 25 °C to 95 °C at 1 °C/min with the fluorescence read six times at each temperature ramp. The resulting data were fit to a Boltzmann sigmoidal equation to determine the melting point of each *Af*FabI construct with and without substrate. Each enzyme or enzyme and substrate condition was replicated six times, and the thermal melting point of each replicate was determined independently. The melting points from each replicate were averaged to determine the reported thermal melting point. A representative thermal shift experiment is shown in Figure 3*D* and average thermal melting points from triplicate experiments are shown in Table 2.

Mass spectrometry analysis of the AfFabI enzyme reaction

Samples were diluted with an equal volume of 80% acetonitrile + 15 mM ammonium hydroxide and were analyzed by direct injection to a QTrap 4500 equipped with a Turbo V ion source (Sciex). The QTrap 4500 was operated in the positive mode using neutral loss scanning, and the ion source parameters were ion spray voltage, 5000 V; curtain gas, 15 psi; temperature, 275 °C; collision gas, medium; ion source gas 1, 15 psi; ion source gas 2, 20 psi; neutral loss, 507.0 *m*/*z*; declustering potential, 50 V; and collision energy, 40 V. The system was controlled and analyzed by the Analyst® software (Sciex).

Crystallization and structure determination

The *Af*FabI protein was concentrated to 12 mg/ml for crystallization. Initial screening was performed at 20 °C against the Protein Complex Suite (Qiagen) by hanging drop vapor diffusion method combining 300 nl protein and 200 nl precipitant. Diffraction quality crystals were obtained by combining 1.5 μl protein and 1 μl 1.2 M sodium potassium tartrate and 100 mM Tris-HCl, pH 8.0. Crystals were cryo-protected with 1.3 M sodium potassium tartrate, 100 mM Tris-HCl, pH 8.0, and 20% v/v glycerol, and then flash-frozen in liquid nitrogen for X-ray diffraction experiments. The diffraction datasets were collected at the SER-CAT beam line 22-ID at the Advanced Photon Source and processed using HKL2000 (69). The *Af*FabI structure was solved by the molecular replacement method using the program Phaser (70) and the coordinates of FabI from *Aquifex aeolicus* (PDB ID: 2P91) (71) as the search model. The *Af*FabI·NADH complex was achieved by incubating 5 mg/ml (150 μM) *Af*FabI with 500 μM NADH for 2 h at room temperature prior to crystallization. Crystals were grown by hanging drop vapor diffusion by combining 1.5 μl of the protein·substrate mixture and 1.5 μl 12.5% PEG 1000, 200 mM NaCl, and 100 mM MES, pH 6.0. Crystals were cryo-protected with 12.5% PEG 1000, 200 mM NaCl, 100 mM MES, pH 6.0, and 25% glycerol, and then flash-frozen in liquid nitrogen for X-ray analysis. Diffraction datasets were collected at the NSLS-II NYX beamline (19-ID) and AMX beamline (17-ID-1) at the Brookhaven National Laboratory and processed using XDS (72). The structure of the *Af*FabI·NADH complex was solved by molecular replacement using the *Af*FabI structure lacking α9 as a search model. The structures were completed by iterative rounds of refinement using REFMAC (73) and manual rebuilding using Coot (74). The refinement was monitored by following the R_{free} value calculated from a random subset (5%) of omitted reflections. A tight turn resolved in the electron density map led to 0.2% of the atoms to be in the Ramachandran outliers (Asn-161^A in the *Af*FabI structure, and Asn-161^A, Asn-161^C in the *Af*FabI·NADH complex structure). A summary of the data processing and structure refinement statistics is provided in Table 1. The coordinates have been deposited in the Protein Data Bank (accession code 6VLX *Af*FabI; 6VLY *Af*FabI·NADH complex). The figures related to the protein structure were generated with PyMOL (75).

In silico analyses

Cα RMSD calculations were performed using SSM Superpose in Coot (74). Surface areas were calculated in PyMOL as described previously (76). The buried surface area by dimerization was calculated by subtracting the surface area of two protomers linked along the *P* axis from the combined surface area of the two individual protomers. The buried surface by tetramerization was calculated by subtracting the surface area of two protomers linked along the *Q* axis from the combined surface area of the two individual protomers. The buried surface area from the helix–helix interaction domain was calculated by subtracting the surface area of two protomers linked along the *R* axis from the combined surface area of the two individual protomers. The water channels and water well were visualized using the PyMOL surface view in Cavities and Pockets (Culled) mode. AFN-1252 binding visualization across FabI clades was done by structural alignment of the catalytic dyads from clade I *Ec*FabI·NAD^+·AFN-1252 (PDB ID: 4JQC) (77), clade II *Mt*InhA·NAD^+ (PDB ID: 4DRE) (78, 82), clade III *Ct*FabI·NADH·AFN-1252 (PDB ID: 4Q9N) (29, 83), and clade IV *Af*FabI·NAD^+ (PDB ID: 6VLY).

Statistical analysis

Statistical analysis (*i.e.* standard error, $K_{0.5}$) and mathematical modeling (*i.e.* Hill equation, variable slope nonlinear regression) were performed using GraphPad Prism software version 8.2.1.

Data availability

Coordinates and structure factors for *Af*FabI and *Af*FabI·NADH crystal structures have been deposited in the Protein Data Bank (PDB) under accession codes 6VLX and 6VLY, respectively. All remaining data are contained within the article.

Author contributions—C. D. R., J. Y., and C. O. R. conceptualization; C. D. R., M. W. F., J. Y., J. S., and D. J. M. data curation; C. D. R., M. W. F., J. Y., J. S., and D. J. M. formal analysis; C. D. R. and C. O. R. investigation; C. D. R., M. W. F., J. S., and D. J. M. methodology; C. D. R. writing-original draft; C. D. R., M. W. F., J. Y., J. S., D. J. M., and C. O. R. writing-review and editing; D. J. M. resources; D. J. M. software; C. O. R. supervision; C. O. R. funding acquisition; C. O. R. project administration.

Acknowledgments—We thank Dr. Amanda Nourse (Molecular Interaction Analysis Shared Resource, St. Jude Children's Research Hospital) for sample analysis by analytical ultracentrifugation and Brett Waddell (Molecular Interaction Analysis Shared Resource, St. Jude Children's Research Hospital) for NADH-binding experiments by surface plasmon resonance. We thank the St. Jude Structural Biology X-ray Center for crystallography support. The Southeast Regional Collaborative Access Team (SER-CAT) 22-ID beamline at the Advanced Photon Source, Argonne National Laboratory is supported by its member institutions, and equipment grants (S10_RR25528 and S10_RR028976) from the National Institutes of Health. Use of the Advanced Photon Source was supported by the U. S. Department of Energy, Office of Science, Office of Basic Energy Sciences, under Contract No. W-31–109-Eng-38. The NYX (19-ID) and AMX (17-ID-1) beamlines of the National Synchrotron Light Source II is a U.S. Department of Energy (DOE) Office of Science User Facility operated for the DOE Office of Science by Brookhaven National Laboratory under Contract DE-SC0012704. NYX is supported by the New York Structural Biology Center (NYSBC). AMX is part of the Center for BioMolecular Structure that is supported by the National Institute of General Medical Sciences (P30 GM133893), and by the DOE Office of Biological and Environmental Research (KP 1605010).

References

1. Parsons, J. B., and Rock, C. O. (2013) Bacterial lipids: Metabolism and membrane homeostasis. *Prog. Lipid Res.* **52,** 249–276 CrossRef Medline
2. Heath, R. J., and Rock, C. O. (2000) A triclosan-resistant bacterial enzyme. *Nature* **406,** 145–146 CrossRef Medline
3. Marrakchi, H., DeWolf, W. E., Jr., Quinn, C., West, J., Polizzi, B. J., So, C. Y., Holmes, D. J., Reed, S. L., Heath, R. J., Payne, D. J., Rock, C. O., and Wallis, N. G. (2003) Characterization of *Streptococcus pneumoniae* enoyl-[acyl carrier protein] reductase (FabK). *Biochem. J.* **370,** 1055–1062 CrossRef Medline
4. Saito, J., Yamada, M., Watanabe, T., Iida, M., Kitagawa, H., Takahata, S., Ozawa, T., Takeuchi, Y., and Ohsawa, F. (2008) Crystal structure of enoyl-acyl carrier protein reductase (FabK) from *Streptococcus pneumoniae* reveals the binding mode of an inhibitor. *Protein Sci.* **17,** 691–699 CrossRef Medline
5. Hevener, K. E., Santarsiero, B. D., Lee, H., Jones, J. A., Boci, T., Johnson, M. E., and Mehboob, S. (2018) Structural characterization of *Porphyromonas gingivalis* enoyl-ACP reductase II (FabK). *Acta Crystallogr. F Struct. Biol. Commun.* **74,** 105–112 CrossRef Medline
6. Oppermann, U., Filling, C., Hult, M., Shafqat, N., Wu, X., Lindh, M., Shafqat, J., Nordling, E., Kallberg, Y., Persson, B., and Jornvall, H. (2003) Short-chain dehydrogenases/reductases (SDR): The 2002 update. *Chem. Biol. Interact.* **143–144,** 247–253 CrossRef Medline
7. White, S. W., Zheng, J., Zhang, Y.-M., and Rock, C. O. (2005) The structural biology of type II fatty acid biosynthesis. *Annu. Rev. Biochem.* **74,** 791–831 CrossRef Medline
8. Baker, M. E. (1995) Enoyl-acyl-carrier-protein reductase and *Mycobacterium tuberculosis* InhA do not conserve the Tyr-*X*aa-*X*aa-*X*aa-Lys motif in mammalian 11β- and 17β-hydroxysteroid dehydrogenases and *Drosophila* alcohol dehydrogenase. *Biochem. J.* **309,** 1029–1030 CrossRef Medline
9. Parikh, S., Moynihan, D. P., Xiao, G., and Tonge, P. J. (1999) Roles of tyrosine 158 and lysine 165 in the catalytic mechanism of InhA, the enoyl-ACP reductase from *Mycobacterium tuberculosis*. *Biochemistry* **38,** 13623–13634 CrossRef Medline
10. Heath, R. J., Su, N., Murphy, C. K., and Rock, C. O. (2000) The enoyl-[acyl-carrier-protein] reductases FabI and FabL from *Bacillus subtilis*. *J. Biol. Chem.* **275,** 40128–40133 CrossRef Medline
11. Kim, K. H., Ha, B. H., Kim, S. J., Hong, S. K., Hwang, K. Y., and Kim, E. E. (2011) Crystal structures of enoyl-ACP reductases I (FabI) and III (FabL) from *B. subtilis*. *J. Mol. Biol.* **406,** 403–415 CrossRef Medline
12. Massengo-Tiassé, R. P., and Cronan, J. E. (2008) *Vibrio cholerae* fabV defines a new class of enoyl acyl-carrier-protein reductase. *J. Biol. Chem.* **283,** 1308–1316 CrossRef Medline
13. Zhu, L., Lin, J., Ma, J., Cronan, J. E., and Wang, H. (2010) Triclosan resistance of *Pseudomonas aeruginosa* PAO1 is due to FabV, a triclosan-resistant enoyl-acyl carrier protein reductase. *Antimicrob. Agents Chemother.* **54,** 689–698 CrossRef Medline
14. Hirschbeck, M. W., Kuper, J., Lu, H., Liu, N., Neckles, C., Shah, S., Wagner, S., Sotriffer, C. A., Tonge, P. J., and Kisker, C. (2012) Structure of the *Yersinia pestis* FabV enoyl-ACP reductase and its interaction with two 2-pyridone inhibitors. *Structure* **20,** 89–100 CrossRef Medline
15. Heath, R. J., and Rock, C. O. (1995) Enoyl-acyl carrier protein reductase (*fabI*) plays a determinant role in completing cycles of fatty acid elongation in *Escherichia coli*. *J. Biol. Chem.* **270,** 26538–26542 CrossRef Medline
16. Yao, J., and Rock, C. O. (2016) Resistance mechanisms and the future of bacterial enoyl-acyl carrier protein reductase (FabI) antibiotics. *Cold Spring Harbor Perspect. Med.* **6,** a027045 CrossRef Medline
17. Yao, J., and Rock, C. O. (2017) Bacterial fatty acid metabolism in modern antibiotic discovery. *Biochim. Biophys. Acta Mol. Cell Biol. Lipids* **1862,** 1300–1309 CrossRef Medline
18. Kaplan, N., Awrey, D., Bardouniotis, E., Berman, J., Yethon, J., Pauls, H. W., and Hafkin, B. (2013) In vitro activity (MICs and rate of kill) of AFN-1252, a novel FabI inhibitor, in the presence of serum and in combination with other antibiotics. *J. Chemother.* **25,** 18–25 CrossRef Medline
19. Kaplan, N., Albert, M., Awrey, D., Bardouniotis, E., Berman, J., Clarke, T., Dorsey, M., Hafkin, B., Ramnauth, J., Romanov, V., Schmid, M. B., Thalakada, R., Yethon, J., and Pauls, H. W. (2012) Mode of action, *in vitro* activity, and *in vivo* efficacy of AFN-1252, a selective antistaphylococcal FabI inhibitor. *Antimicrob. Agents Chemother.* **56,** 5865–5874 CrossRef Medline
20. Hafkin, B., Kaplan, N., and Murphy, B. (2015) Efficacy and safety of AFN-1252, the first *Staphylococcus*-specific antibacterial agent, in the treatment of acute bacterial skin and skin structure infections, including those in patients with significant comorbidities. *Antimicrob. Agents Chemother.* **60,** 1695–1701 CrossRef Medline
21. Menetrey, A., Janin, A., Pullman, J., Overcash, J. S., Haouala, A., Leylavergne, F., Turbe, L., Wittke, F., and Nicolas-Métral, V. (2019) Bone and joint tissue penetration of the *Staphylococcus*-selective antibiotic afabicin in patients undergoing elective hip replacement surgery. *Antimicrob. Agents Chemother.* **63,** e01669-18 CrossRef Medline
22. Keeney, K. M., Yurist-Doutsch, S., Arrieta, M. C., and Finlay, B. B. (2014) Effects of antibiotics on human microbiota and subsequent disease. *Annu. Rev. Microbiol.* **68,** 217–235 CrossRef Medline
23. Croswell, A., Amir, E., Teggatz, P., Barman, M., and Salzman, N. H. (2009) Prolonged impact of antibiotics on intestinal microbial ecology and susceptibility to enteric *Salmonella* infection. *Infect. Immun.* **77,** 2741–2753 CrossRef Medline
24. Yao, J., Carter, R. A., Vuagniaux, G., Barbier, M., Rosch, J. W., and Rock, C. O. (2016) A pathogen-selective antibiotic minimizes disturbance to the microbiome. *Antimicrob. Agents Chemother.* **60,** 4264–4273 CrossRef Medline
25. Rinninella, E., Raoul, P., Cintoni, M., Franceschi, F., Miggiano, G. A. D., Gasbarrini, A., and Mele, M. C. (2019) What is the healthy gut microbiota composition? A changing ecosystem across age, environment, diet, and diseases. *Microorganisms* **7,** E14 CrossRef Medline
26. Ward, W. H., Holdgate, G. A., Rowsell, S., McLean, E. G., Pauptit, R. A., Clayton, E., Nichols, W. W., Colls, J. G., Minshull, C. A., Jude, D. A.,

Mistry, A., Timms, D., Camble, R., Hales, N. J., Britton, C. J., and Taylor, I. W. (1999) Kinetic and structural characteristics of the inhibition of enoyl (acyl carrier protein) reductase by triclosan. *Biochemistry* **38,** 12514–12525 CrossRef Medline

27. Schiebel, J., Chang, A., Lu, H., Baxter, M. V., Tonge, P. J., and Kisker, C. (2012) *Staphylococcus aureus* FabI: Inhibition, substrate recognition, and potential implications for *in vivo* essentiality. *Structure* **20,** 802–813 CrossRef Medline
28. Rozwarski, D. A., Vilchèze, C., Sugantino, M., Bittman, R., and Sacchettini, J. C. (1999) Crystal structure of the *Mycobacterium tuberculosis* enoyl-ACP reductase, InhA, in complex with NAD^+ and a C16 fatty acyl substrate. *J. Biol. Chem.* **274,** 15582–15589 CrossRef Medline
29. Yao, J., Abdelrahman, Y. M., Robertson, R. M., Cox, J. V., Belland, R. J., White, S. W., and Rock, C. O. (2014) Type II fatty acid synthesis is essential for the replication of *Chlamydia trachomatis*. *J. Biol. Chem.* **289,** 22365–22376 CrossRef Medline
30. Belluti, F., Perozzo, R., Lauciello, L., Colizzi, F., Kostrewa, D., Bisi, A., Gobbi, S., Rampa, A., Bolognesi, M. L., Recanatini, M., Brun, R., Scapozza, L., and Cavalli, A. (2013) Design, synthesis, and biological and crystallographic evaluation of novel inhibitors of *Plasmodium falciparum* enoyl-ACP-reductase (*Pf*FabI). *J. Med. Chem.* **56,** 7516–7526 CrossRef Medline
31. Johnson, E. L., Heaver, S. L., Walters, W. A., and Ley, R. E. (2017) Microbiome and metabolic disease: Revisiting the bacterial phylum Bacteroidetes. *J. Mol. Med. (Berl.)* **95,** 1–8 CrossRef Medline
32. Karlowsky, J. A., Kaplan, N., Hafkin, B., Hoban, D. J., and Zhanel, G. G. (2009) AFN-1252, a FabI inhibitor, demonstrates a *Staphylococcus*-specific spectrum of activity. *Antimicrob. Agents Chemother.* **53,** 3544–3548 CrossRef Medline
33. Yao, J., Maxwell, J. B., and Rock, C. O. (2013) Resistance to AFN-1252 arises from missense mutations in *Staphylococcus aureus* enoyl-acyl carrier protein reductase (FabI). *J. Biol. Chem.* **288,** 36261–36271 CrossRef Medline
34. Heath, R. J., Li, J., Roland, G. E., and Rock, C. O. (2000) Inhibition of the *Staphylococcus aureus* NADPH-dependent enoyl-acyl carrier protein reductase by triclosan and hexachlorophene. *J. Biol. Chem.* **275,** 4654–4659 CrossRef Medline
35. Heath, R. J., Rubin, J. R., Holland, D. R., Zhang, E., Snow, M. E., and Rock, C. O. (1999) Mechanism of triclosan inhibition of bacterial fatty acid synthesis. *J. Biol. Chem.* **274,** 11110–11114 CrossRef Medline
36. Jordan, C. A., Sandoval, B. A., Serobyan, M. V., Gilling, D. H., Groziak, M. P., Xu, H. H., and Vey, J. L. (2015) Crystallographic insights into the structure-activity relationships of diazaborine enoyl-ACP reductase inhibitors. *Acta Crystallogr. F Struct. Biol. Cryst. Commun.* **71,** 1521–1530 CrossRef Medline
37. Marrakchi, H., Choi, K.-H., and Rock, C. O. (2002) A new mechanism for anaerobic unsaturated fatty acid formation in *Streptococcus pneumoniae*. *J. Biol. Chem.* **277,** 44809–44816 CrossRef Medline
38. Kim, H. T., Kim, S., Na, B. K., Chung, J., Hwang, E., and Hwang, K. Y. (2017) Structural insights into the dimer-tetramer transition of FabI from *Bacillus anthracis*. *Biochem. Biophys. Res. Commun.* **493,** 28–33 CrossRef Medline
39. Kim, S. J., Ha, B. H., Kim, K. H., Hong, S. K., Shin, K. J., Suh, S. W., and Kim, E. E. (2010) Dimeric and tetrameric forms of enoyl-acyl carrier protein reductase from *Bacillus cereus*. *Biochem. Biophys. Res. Commun.* **400,** 517–522 CrossRef Medline
40. Priyadarshi, A., Kim, E. E., and Hwang, K. Y. (2010) Structural insights into *Staphylococcus aureus* enoyl-ACP reductase (FabI), in complex with NADP and triclosan. *Proteins* **78,** 480–486 CrossRef Medline
41. Rafferty, J. B., Simon, J. W., Baldock, C., Artymiuk, P. J., Baker, P. J., Stuitje, A. R., Slabas, A. R., and Rice, D. W. (1995) Common themes in redox chemistry emerge from the X-ray structure of oilseed rape (*Brassica napus*) enoyl acyl carrier protein reductase. *Structure* **3,** 927–938 CrossRef Medline
42. Perozzo, R., Kuo, M., Sidhu, A. S., Valiyaveettil, J. T., Bittman, R., Jacobs, W. R., Jr., Fidock, D. A., and Sacchettini, J. C. (2002) Structural elucidation of the specificity of the antibacterial agent triclosan for malarial enoyl acyl carrier protein reductase. *J. Biol. Chem.* **277,** 13106–13114 CrossRef Medline
43. Luckner, S. R., Liu, N., am Ende, C. W., Tonge, P. J., and Kisker, C. (2010) A slow, tight binding inhibitor of InhA, the enoyl-acyl carrier protein reductase from *Mycobacterium tuberculosis*. *J. Biol. Chem.* **285,** 14330–14337 CrossRef Medline
44. Pidugu, L. S., Kapoor, M., Surolia, N., Surolia, A., and Suguna, K. (2004) Structural basis for the variation in triclosan affinity to enoyl reductases. *J. Mol. Biol.* **343,** 147–155 CrossRef Medline
45. Ghosh, D., Wawrzak, Z., Weeks, C. M., Duax, W. L., and Erman, M. (1994) The refined three-dimensional structure of 3α,20β-hydroxysteroid dehydrogenase and possible roles of the residues conserved in short-chain dehydrogenases. *Structure* **2,** 629–640 CrossRef Medline
46. Tanaka, N., Nonaka, T., Tanabe, T., Yoshimoto, T., Tsuru, D., and Mitsui, Y. (1996) Crystal structures of the binary and ternary complexes of 7α-hydroxysteroid dehydrogenase from *Escherichia coli*. *Biochemistry* **35,** 7715–7730 CrossRef Medline
47. Hol, W. G., van Duijnen, P. T., and Berendsen, H. J. (1978) The α-helix dipole and the properties of proteins. *Nature* **273,** 443–446 CrossRef Medline
48. Muench, S. P., Prigge, S. T., McLeod, R., Rafferty, J. B., Kirisits, M. J., Roberts, C. W., Mui, E. J., and Rice, D. W. (2007) Studies of *Toxoplasma gondii* and *Plasmodium falciparum* enoyl acyl carrier protein reductase and implications for the development of antiparasitic agents. *Acta Crystallogr. D Biol. Crystallogr.* **63,** 328–338 CrossRef Medline
49. Qiu, X., Janson, C. A., Court, R. I., Smyth, M. G., Payne, D. J., and Abdel-Meguid, S. S. (1999) Molecular basis for triclosan activity involves a flipping loop in the active site. *Protein Sci.* **8,** 2529–2532 CrossRef Medline
50. Dessen, A., Quémard, A., Blanchard, J. S., Jacobs, W. R., Jr., and Sacchettini, J. C. (1995) Crystal structure and function of the isoniazid target of *Mycobacterium tuberculosis*. *Science* **267,** 1638–1641 CrossRef Medline
51. Mehboob, S., Hevener, K. E., Truong, K., Boci, T., Santarsiero, B. D., and Johnson, M. E. (2012) Structural and enzymatic analyses reveal the binding mode of a novel series of *Francisella tularensis* enoyl reductase (FabI) inhibitors. *J. Med. Chem.* **55,** 5933–5941 CrossRef Medline
52. Schiebel, J., Chang, A., Merget, B., Bommineni, G. R., Yu, W., Spagnuolo, L. A., Baxter, M. V., Tareilus, M., Tonge, P. J., Kisker, C., and Sotriffer, C. A. (2015) An ordered water channel in *Staphylococcus aureus* FabI: Unraveling the mechanism of substrate recognition and reduction. *Biochemistry* **54,** 1943–1955 CrossRef Medline
53. Flocco, M. M., and Mowbray, S. L. (1994) Planar stacking interactions of arginine and aromatic side-chains in proteins. *J. Mol. Biol.* **235,** 709–717 CrossRef Medline
54. Rozwarski, D. A., Grant, G. A., Barton, D. H., Jacobs, W. R., Jr., and Sacchettini, J. C. (1998) Modification of the NADH of the isoniazid target (InhA) from *Mycobacterium tuberculosis*. *Science* **279,** 98–102 CrossRef Medline
55. Langdon, A., Crook, N., and Dantas, G. (2016) The effects of antibiotics on the microbiome throughout development and alternative approaches for therapeutic modulation. *Genome Med.* **8,** 39 CrossRef Medline
56. Francino, M. P. (2015) Antibiotics and the human gut microbiome: Dysbioses and accumulation of resistances. *Front. Microbiol.* **6,** 1543 CrossRef Medline
57. Schliep, K. P. (2011) Phangorn: Phylogenetic analysis in R. *Bioinformatics* **27,** 592–593 CrossRef Medline
58. Wright, E. S. (2015) DECIPHER: Harnessing local sequence context to improve protein multiple sequence alignment. *BMC Bioinformatics* **16,** 322 CrossRef Medline
59. Le, S. Q., and Gascuel, O. (2008) An improved general amino acid replacement matrix. *Mol. Biol. Evol.* **25,** 1307–1320 CrossRef Medline
60. Yu, G. C., Smith, D. K., Zhu, H. C., Guan, Y., and Lam, T. T. Y. (2017) GGTREE: An R package for visualization and annotation of phylogenetic trees with their covariates and other associated data. *Methods Ecol. Evol.* **8,** 28–36 CrossRef
61. Radka, C. D., Frank, M. W., Rock, C. O., and Yao, J. (2020) Fatty acid activation and utilization by *Alistipes finegoldii*, a representative Bacteroidetes resident of the human gut microbiome. *Mol. Microbiol.* **113,** 807–825 CrossRef Medline
62. Parsons, J. B., Frank, M. W., Subramanian, C., Saenkham, P., and Rock, C. O. (2011) Metabolic basis for the differential susceptibility of Gram-

positive pathogens to fatty acid synthesis inhibitors. *Proc. Natl. Acad. Sci. U.S.A.* **108,** 15378–15383 CrossRef Medline
63. Jackowski, S., Zhang, Y.-M., Price, A. C., White, S. W., and Rock, C. O. (2002) A missense mutation in the *fabB* (β-ketoacyl-acyl carrier protein synthase I) gene confers thiolactomycin resistance to *Escherichia coli*. *Antimicrob. Agents Chemother.* **46,** 1246–1252 CrossRef Medline
64. Zhao, H., Brautigam, C. A., Ghirlando, R., and Schuck, P. (2013) Overview of current methods in sedimentation velocity and sedimentation equilibrium analytical ultracentrifugation. *Curr. Protoc. Protein Sci.* **71,** 20.12.1–20.12.49 CrossRef Medline
65. Schuck, P., Brautigam, Z. H. C. A., and Ghirlando, R. (2015) *Basic Principles of Analytical Ultracentrifugation*, CRC Press, Inc., Boca Raton, FL.
66. Schuck, P. (2000) Size-distribution analysis of macromolecules by sedimentation velocity ultracentrifugation and Lamm equation modeling. *Biophys. J.* **78,** 1606–1619 CrossRef Medline
67. Zhao, H., Ghirlando, R., Alfonso, C., Arisaka, F., Attali, I., Bain, D. L., Bakhtina, M. M., Becker, D. F., Bedwell, G. J., Bekdemir, A., Besong, T. M., Birck, C., Brautigam, C. A., Brennerman, W., Byron, O., *et al.* (2015) A multilaboratory comparison of calibration accuracy and the performance of external references in analytical ultracentrifugation. *PLoS One* **10,** e0126420 CrossRef Medline
68. Yao, J., Bruhn, D. F., Frank, M. W., Lee, R. E., and Rock, C. O. (2016) Activation of exogenous fatty acids to acyl-acyl carrier protein cannot bypass FabI inhibition in *Neisseria*. *J. Biol. Chem.* **291,** 171–181 CrossRef Medline
69. Otwinowski, Z., and Minor, W. (1997) [20] Processing of X-ray diffraction data collected in oscillation mode. *Methods Enzymol.* **276,** 307–326 CrossRef Medline
70. McCoy, A. J. (2007) Solving structures of protein complexes by molecular replacement with Phaser. *Acta Crystallogr. D Biol. Crystallogr.* **63,** 32–41 CrossRef Medline
71. Chen, L., Li, Y., Ebihara, A., Shinkai, A., Kuramitsu, S., Yokoyama, S., Zhao, M., Rose, J. P., Wang, B. C., Southeast Collaboratory for Structural Genomics (SECSG), and RIKEN Structural Genomics/Proteomics Initiative (RSGI). (2007) Crystal structure of enoyl-[acyl-carrier-protein] reductase (NADH) from *Aquifex aeolicus* VF5. Protein Data Bank. 2P91
72. Kabsch, W. (2010) XDS. *Acta Crystallogr. D Biol. Crystallogr.* **66,** 125–132 CrossRef Medline
73. Skubák, P., Murshudov, G. N., and Pannu, N. S. (2004) Direct incorporation of experimental phase information in model refinement. *Acta Crystallogr. D Biol. Crystallogr.* **60,** 2196–2201 CrossRef Medline
74. Emsley, P., and Cowtan, K. (2004) Coot: Model-building tools for molecular graphics. *Acta Crystallogr. D Biol. Crystallogr.* **60,** 2126–2132 CrossRef Medline
75. DeLano, W. L. (2002) *The PyMOL Molecular Graphics System*. DeLano Scientific, Palo Alto, CA
76. Radka, C. D., Chen, D., DeLucas, L. J., and Aller, S. G. (2017) The crystal structure of the *Yersinia pestis* iron chaperone YiuA reveals a basic triad binding motif for the chelated metal. *Acta Crystallogr. D Struct. Biol.* **73,** 921–939 CrossRef Medline
77. Subramanya, H., Rao, K. N., and Anirudha, L. (2013) Crystal structure of *E. coli* enoyl reductase in complex with NAD and AFN-1252. Protein Data Bank. 4JQC
78. Hartkoorn, R. C., Sala, C., Neres, J., Pojer, F., Magnet, S., Mukherjee, R., Uplekar, S., Boy-Röttger, S., Altmann, K. H., and Cole, S. T. (2012) Towards a new tuberculosis drug: Pyridomycin—nature's isoniazid. *EMBO Mol. Med.* **4,** 1032–1042 CrossRef Medline
79. Bergler, H., Hogenauer, G., and Turnowsky, F. (1992) Sequences of the *envM* gene and of two mutated alleles in *Escherichia coli*. *J. Gen. Microbiol.* **138,** 2093–2100 CrossRef Medline
80. Lu, Y.-J., Zhang, Y.-M., Grimes, K. D., Qi, J., Lee, R. E., and Rock, C. O. (2006) Acyl-phosphates initiate membrane phospholipid synthesis in gram-positive pathogens. *Molec. Cell* **23,** 765–772 CrossRef Medline
81. Jordan, C. A., and Vey, J. L. (2015) Crystal structure of *E. coli* FabI in apo form. Protein Data Bank. 5CFZ
82. Pojer, F., Hartkoorn, R.C., Boy. S., Cole, S.T. (2012) Mycobacterium tuberculosis InhA in complex with NADH. Protein Data Bank. 4DRE
83. Yao, J., Abdelrahman, Y., Robertson, R.M., Cox, J.V., Belland, R.J., White, S.W., Rock, C.O. (2014) Crystal structure of *Chlamydia trachomatis* enoyl-ACP reductase (FabI) in complex with NADH and AFN-1252. Protein Data Bank. 4Q9N